Amorphous selenium (a-Se) avalanche photodetector for applications in Positron Emission Tomography (PET)

By

OLEKSANDR BUBON

Master of Science in Physics

Lakehead University

Thunder Bay, Ontario

2011

Amorphous selenium (a-Se) avalanche photodetector for applications in Positron Emission Tomography (PET)

Master of Science, 2011

Oleksandr Bubon

Department of Physics

Lakehead University

Abstract

Although avalanche amorphous selenium (a-Se) is a very promising photoconductor for a variety of imaging applications, it is currently restricted to applications with electron beam readout. This is performed with a vacuum pick-up tube called a High-gain Avalanche Rushing Photoconductor (HARP) Vidicon. The electron beam readout is compatible with high definition television (HDTV) applications, but for use in medical imaging devices it should be replaced by an solid-state electronic readout with a two-dimensional array of metal pixel electrodes. However, due to the high electric field required for avalanche multiplication, it is a technological challenge to avoid dielectric breakdown at the edges, where electric field experiences local enhancement. We show that this problem can be overcome by the use of a *Resistive Interface Layer* (RIL) deposited between the uniform a-Se layer and the array of metal electrodes. By detailed analysis of charge transport properties we demonstrate that RIL enables stable avalanche operation in a-Se photoconductor without degradation in charge transport or avalanche multiplication gain. Our results showed that a stable gain of 200 is reached at 104 V/μm for a 15-μm thick a-Se layer, which is the maximum theoretical gain for this thickness. We conclude that RIL is an enabling technology for practical implementation of solid-state avalanche a-Se image sensors.

Acknowledgements

I would like to thank Dr. Alla Reznik for providing me with excellent guidance and scientific training over the past two years in Department of Physics at Lakehead University. Her encouragement during trying times always gave me renewed hope and strength to persevere. I also want to thank my supervisory committee members, Dr. Guatam Das and Dr. John Rowlands, for their advice. Although the questions during committee meetings seemed tough at the time, they help me develop a more mature and scientifically-sound way of thinking.

I extend my appreciation to Giovanni DeCrescenzo and Sergey Reznik for their help with the experiments and for the interesting and helpful discussions on amorphous selenium.

Table of Contents

List of Figures

List of Acroyms

ACD	Annihilation Coincidence Detection
APD	Avalanche Photodiode
ATPs	Adenosine Triphosphates
BGO	Bismuth Germinate
CCT	Charge-Collection Time
CT	X–ray Computed Tomography
DOI	Depth-of-Interaction
EHP	Electron-hole-Pair
FDG	2-fluoro-2-deoxy-D-glucose
FOV	Field of View
FWHM	Full Width Half Maximum
HARP	High-gain Avalanche Rushing Photoconductor
HCFA	Health Care Financing Administration
ITO	Indium Tin Oxide
LOR	Line of Response
LSO	Lutetium Oxyorthosilicate
LYSO	Lutetium-Yttrium Oxyorthosilicate
MGH	Massachusetts General Hospital
MRI	Magnetic Resonance Imaging
OCT	Optical Coherent Tomography
PEM	Positron Emission Mammography
PET	Positron Emission Tomography
PMT	Photomultiplier Tube
QE	Quantum Efficiency
SI	Systeme International

SNR	Sigmal to Noise Ratio
SPECT	Single Photon Emission Computed Tomography
TFT	Thin Film Transistor
TOF	Time of flight
TTS	Transit-Time Spread
WB	Whole Body

Chapter 1 Introduction

1.1.A brief history of PET

The field of medical imaging includes many different imaging modalities (Table 1.1) A significant role is taken by the Positron Emission Tomography (PET) systems, as PET is a medical imaging technique that provides functional images of the body, which plays an important role in cancer diagnosis and treatment. Table 1.1 show main advantages and disadvantages of different key imaging modalities.

Table 1.1. Summary of the advantages and disadvantages of key imaging modalities [1].

Modality	Advantages	Disadvantages
X-ray fluoroscopy	• high spatial resolution • high temporal resolution • excellent geometrical accuracy • low relative cost	• ionizing radiation • poor soft tissue contrast • not tomographic
Ultrasound	• high temporal resolution • no ionizing radiation • low relative cost • localized imaging can be performed at catheter tip • tomographic	• poor spatial resolution • poor imaging performance near bones and air-filled cavities • large operator dependency
MRI	• good soft tissue contrast • no ionizing radiation • localized imaging can be performed at catheter tip • tomographic	• requires specialized non-magnetic devices • fundamental tradeoff between image quality and temporal resolution • very high cost
OCT	• high spatial resolution • high temporal resolution • low relative cost • tomographic	• limited to localized imaging at catheter tip
PET	• measures the metabolic activity of cells • produces molecular images • demonstrates pathological changes faster	• ionizing radiation • spatial resolution needs to be improved • high cost • requires a cyclotron nearby

The only imaging modality which can provide information about metabolic activity in the patient body is PET. So it is called functional imaging and commonly used for cancer detection.

The first use of positrons in a medical imaging application dates back to 1950, when William H. Sweet and Gordon L. Brownell used positron annihilation to investigate brain tumors at the Physics Research Laboratory of the Massachusetts General Hospital (MGH). In that time their positron imaging system consisted simply of two opposing detectors eachmade of a single sodium iodide (NaI:TI) crystal and photomultiplier. Two dimensional images were obtained by mechanically translating the detector pair in two orthogonal directions perpendicular to the path of the annihilation photons [2]. It was immediately used for patient imaging with brain tumors, and the results were published in the New England Journal of Medicine [3]. Wrenn *et al*. also published independent work on a similar use of positrons for localizing brain tumors in the same year [4].

Within the next 20 years, positron imaging evolved into a tomographic imaging method with the development of reconstruction algorithms. The reconstruction technique used in PET imaging is very similar to that used in CT scanners. The first tomographic positron scanners were built in the 1970s. These first generation PET scanners were much simpler than today's commercial systems. For example, PET III, the first human PET scanner developed at Washington University by Michael E. Phelps and colleagues in 1974 [5], had only 48 NaI:TI detectors, each 50 mm in diameter, arranged in a single hexagonal ring. On the other hand, today's scanners have ~10,000 detectors that have dimensions on the order of 5x5 mm^2, arranged in 20-30 detector rings. However, evolution of PET scanners has involved many other important advances both in detector design and PET – related technologies.

The first significant improvement in detector design over the past 30 years is the use of bismuth germinate (BGO) as the scintillation crystal (1978) and the second significant improvement was the invention of the block detector in 1984. In the early 1970s.We will now expand on these two important improvements.

NaI:TI crystals were first used as the scintillator. It had a high light output but its low effective atomic number and low density resulted in a long attenuation length for the 511 keV annihilation photons. It also has a relatively low probability of photoelectric absorption compared to Compton scattering. Furthermore, NaI:TI crystals must be hermetically sealed because they are hygroscopic. BGO, on the other hand is not hygroscopic. BGOhas a higher effective atomic number and almost double the density of NaI:Tl. This resulted in attenuation length of only one-third that of NaI:TI, which permits reduction in detector size. In addition, the probability of photoelectric absorption is more than double that of NaI:TI. Although BGO has a lower light yield and a longer decay time (Table 1.2), the benefits of BGO enable the detector to achieve much higher γ–ray detection efficiency, making BGO the most widely used scintillator in current commercial PET scanners. Table 1.2 shows a comparison of the characteristics of NaI:TI and BGO. BGO has several additional strong advantages over NaI:TI scintillator which has contributed tothe more common use of BGO. A more detailed discussion on scintillation crystals is presented in Section 1.3.3.1.

Table 1.2: Properties of BGO compared with NaI:TI. Data obtained from Melcher [6]

Scintillator	**BGO**	**NaI:TI**
Composition	$BI_4Ge_3O_{12}$	NaI:TI
Effective Atomic Number	**75**	51
Density (g/cm^3)	**7.13**	3.67
Decay time (ns)	300	**230**
Light Yield (photons/MeV)	9,000	**41,000**
Hygroscopic	**No**	Yes
Rugged	**Yes**	No

An important improvement in PET systems was made possible by the invention of the block detector module. This allowed the advance from PET scanners with a few pixels to PET scanners with a few thousand pixels. Before block detectors, each pixel consisted of a photomultiplier tube (PMT) optically coupled to a single scintillation crystal. It started

to be clear that to reach improvement in the spatial resolution of PET images, the size of the pixels must be reduced and the number of pixels must be increased. Several designs were proposed in order to reach this goal, but the most successful was the block detector designed by Casey and Nutt [7]. The block detector was able to achieve this goal while keeping the number of PMTs low as well as the corresponding cost. A more detailed description of the block detector is presented in Section 1.3.3.3.

The performance of PET scanners was increased by improvements in detector technologies, which made possible an increase in diagnostic capability of PET. However, developments in PET radiopharmaceuticals are also critical for the increasing application of PET. Radiotracers used in PET are commonly synthesized with ^{11}C, ^{13}N, ^{15}O and ^{18}F, and are used for imaging glucose uptake, blood flow, oxygen utilization, and bone scans, respectively [8]. Among these, the most valuable radiopharmaceutical, first synthesized in 1978 [9], is the glucose-analogue 2-fluoro-2-deoxy-D-glucose (FDG). FDG is used in PET to image glucose metabolism. FDG, together with the advances in PET detector design, encouraged many PET studies to be performed. The results indicated the value of FDG PET imaging in oncology, cardiology and neurology [10]. Eventually, the Health Care Financing Administration (HCFA) started reimbursing a number of PET procedures in the USA beginning in 1998. Since then, the HCFA has broadened its coverage on PET procedures for different types of cancers, neurological disorders and cardiovascular diseases, further increasing the interest and clinical use of PET.

1.2. FDG PET in oncology

The knowledge that metabolism of many types of tumor cells differs from normal cells has been known for decades. In particular, the glucose uptake in tumor cells was found to be much higher compared to normal cells. Also, the level of glucose metabolism was found to correspond to the degree of malignancy of the tumors. The increase in the glycolytic rate is attributed to the fact that the metabolism of tumor cells is primarily anaerobic. In anaerobic metabolism, the consumption of each glucose molecule produces energy in the form of 2 adenosine triphosphate molecules (ATPs). On the other hand, the more efficient aerobic metabolism of glucose produces up to 36 ATPs per glucose

molecule. Therefore, a tremendous increase in glucose consumption is required in order to produce the same amount of ATPs in cells that rely on anaerobic metabolism. Therefore, by monitoring levels of glucose uptake in the body, malignant tumors can be located and differentiated from benign lesions.

To monitor glucose metabolism, the radiolabelled glucose analogue FDG was designed in 1978 [9]. It is made by replacing one of the hydroxyl groups in glucose with a positron emitting fluorine isotope, ^{18}F. When FDG is introduced into a patient, usually by intravenous injection, the tracer is transported in the circulation like glucose and is taken up by cells. Inside a cell, FDG is phosphorylated by hexokinase, forming FDG-6-phosphate. However, unlike glucose-6-phosphate, FDG-6-phosphate cannot continue in the glycolytic pathway and is effectively trapped in the cell. By detecting the radioactive decay of these trapped FDG molecules, a PET image shows their distribution in the body and provides clues to the location of tumors.

In contrast to conventional imaging modalities such as x–ray computed tomography (CT) and magnetic resonance imaging (MRI), PET is a functional imaging modality which shows the physiology of the human body (Table 1.1). As such, it has several advantages over anatomical imaging. With anatomical images, it is often difficult to assess whether a suspected lesion is malignant just by its size and shape. Lesions may also be obscured by post-treatment anatomical changes, such as scarring and necrosis. PET, on the other hand, provides clinicians with physiological information about suspected lesions and is therefore not affected by anatomical abnormalities. Furthermore, since physiological changes occur before anatomical changes, PET has the potential to reveal tumors at an earlier stage, possibly allowing curative treatment and increasing the chance of survival for the patient. To improve diagnostic capabilities of conventional PET scanners they are combined with CT scanner.

Therefore, PET has many applications in oncology, including diagnosis, staging, distant metastases detection, and treatment response evaluation. Gambhir *et al*. [10] summarized the PET literature in oncology published between 1993 and 2000 and estimated FDG PET sensitivity and specificity to be 84% and 88%, respectively, across different

oncologic applications. It is also estimated that PET has changed patient management in 30-40% of the cases, showing the importance of the information obtained from PET studies.

1.3. Physics of PET

1.3.1. Positron emission

1.3.1.1. Radioactive decay

A *radionuclide* is an atom with an unstable nucleus which spontaneously undergoes *radioactive decay* to achieve a more stable nuclear state. The radionuclide is called the *parent*, and the atom after radioactive decay is called the *daughter*. There are different methods of decay, depending on the type of the radionuclide. The decay of interest in PET is *positron emission*, where a positron, an anti-particle of an electron with the same mass and opposite charge, is emitted. In the positron emission process, a proton (p) is the parent element converted into a neutron (n), a positron (e^+), and a neutrino (ν) and in the process the element X changes to element Y:

$$ {}^{A}_{Z}X \rightarrow {}^{A}_{Z-1}Y + e^{+} + \nu , \tag{1.1} $$

where Z and A are respectively the atomic number and mass of the elementary atoms. With the loss of a proton, the parent, X, is converted into a different element, Y. The energy released depends on the atomic mass and the nuclear states of the parent and daughter. This energy is randomly shared as kinetic energy between the products of the decay. Thus, the positron emitted from the nucleus may take on a range of kinetic energy with a maximum of E_{max}, which is the total energy released by the decay.

Radionuclides that decay by positron emission may also decay by another method called *electron capture*. Although the parent and daughter are the same as in positron emission, the proton in electron capture is converted into a neutron by capturing an orbital electron:

$$ {}^{A}_{Z}X + e^{-} \rightarrow {}^{A}_{Z-1}Y + \nu , \tag{1.2} $$

The vacancy caused by the loss of an electron will be filled by electrons from the outer shells, resulting in emission of one or more x–rays. Positron emission and electron capture are competing processes; radionuclides with a low atomic number tend to decay by positron emission, whereas those with a higher atomic number tend to decay by electron capture.

Radioactive decay is a random process; it is impossible to predict when a given radionuclide will decay. However, all the atoms of the same type of radionuclide have the same probability of undergoing decay at any given time. Therefore, the number of radioactive decays, *dN*, over a given time, *dt*, is expected to be proportional to the total

number of radionuclides, *N*:

$$\frac{dN}{dt} = -\lambda N \,, \tag{1.3}$$

where λ is known as the *decay* constant for that particular type of radionuclide. Solving this differential equation reveals that radioactive decay is an exponential process:

$$N(t) = N(0)e^{-\lambda t} \,, \tag{1.4}$$

where *N(0)* is the initial number of radionuclides, and *N(t)* is the number of remaining radionuclides after time *t*. Instead of the decay constant, the decay of a radionuclide is more commonly characterized by its *half-life*, $t_{1/2}$, which is the time required for 50% of the radionuclides to decay:

$$t_{1/2} = \frac{\ln 2}{\lambda} \tag{1.5}$$

Radioactivity, or simply *activity*, of a sample of radionuclides refers to the number of radioactive decays, or disintegrations, per unit time. The Systeme International (SI) unit for activity is the *Becquerel* (Bq), which is defined as one disintegration per second (dps). Another commonly used unit is the *Curie* (Ci), which is equal to 3.7 x 10^{10} Bq.

1.3.1.2. Annihilation

Positrons emitted in matter lose most of their kinetic energy by ionizing and exciting the surrounding atoms. When a positron has lost most of its kinetic energy, it can no longer prevent the attraction of the surrounding oppositely charged electrons and when they come close enough they undergo mutual annihilation. In this process the entire mass of the electron-positron pair is converted into two γ-rays photons.

Because of the conservation of energy, the total energy of the annihilation photons is given by:

$$E = mc^2 = (m_{e^+} + m_{e^-}) \cdot c^2, \tag{1.6}$$

The mass of both the positron and electron (m_e+ and m_e-) is 9.1×10^{-31} kg, and c, the speed of light, is 3×10^8 m/s. Therefore, the total energy of the photons must be 1.022 MeV. Since the net momentum of the positron and electron is close to zero, the momentum of the final products must be the same; the emission of at least two photons is required for the conservation of momentum. If only one photon is emitted, there will be a net momentum in the direction of that photon, and the initial and final momenta of the annihilation process will be unbalanced. The emission of two photons of the same energy (1.022 MeV/2 = 511 keV) that are 180° apart ensures that both the momentum and the energy are conserved. Although the origin of these energetic photons is not the nucleus, the terms γ–rays and annihilation photons are often used interchangeably (Figure 1.1).

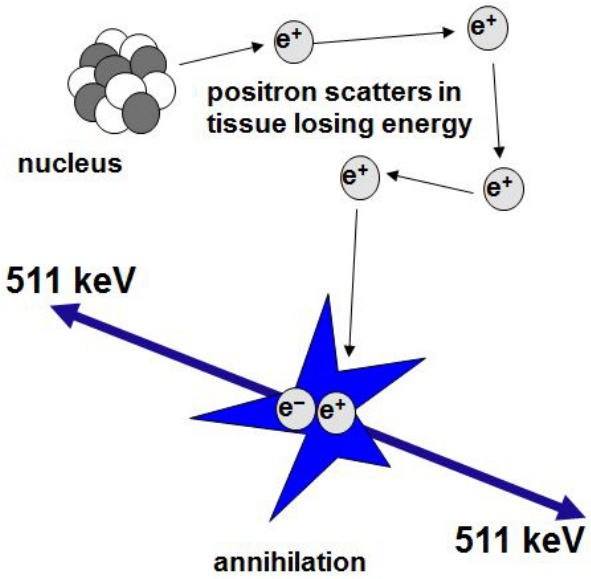

Figure 1.1: After a positron is emitted from the nucleus, it interacts with surrounding atoms and loses its kinetic energy. Then it interacts with an electron resulting in annihilation.

The unique property of opposite γ–ray emission provide PET with big advantages over single-photon imaging methods (e.g. Single Photon Emission Computed Tomography, or SPECT). It permits a process called electronic collimation. First let us consider the inferior method used in SPECT which is conventional collimation. Figure 1.2 shows a schematic of single-photon imaging. Without collimation, it is impossible to determine the origin of the photon when it is detected. To form an image, a physical collimator that absorbs photons must be used. The parallel openings of a collimator allow only those photons close to a single direction to reach the detector, thereby forming a projection image. The conventional collimator is a significant drawback for single-photon imaging, because it reduces the number of detectable photons, by a very considerable amount, 3 orders of magnitude, depending on the resolution desired. This loss of photons means that the statistical noise in the formation is very large unless a correspondingly large dose of radiopharmaceutical is used.

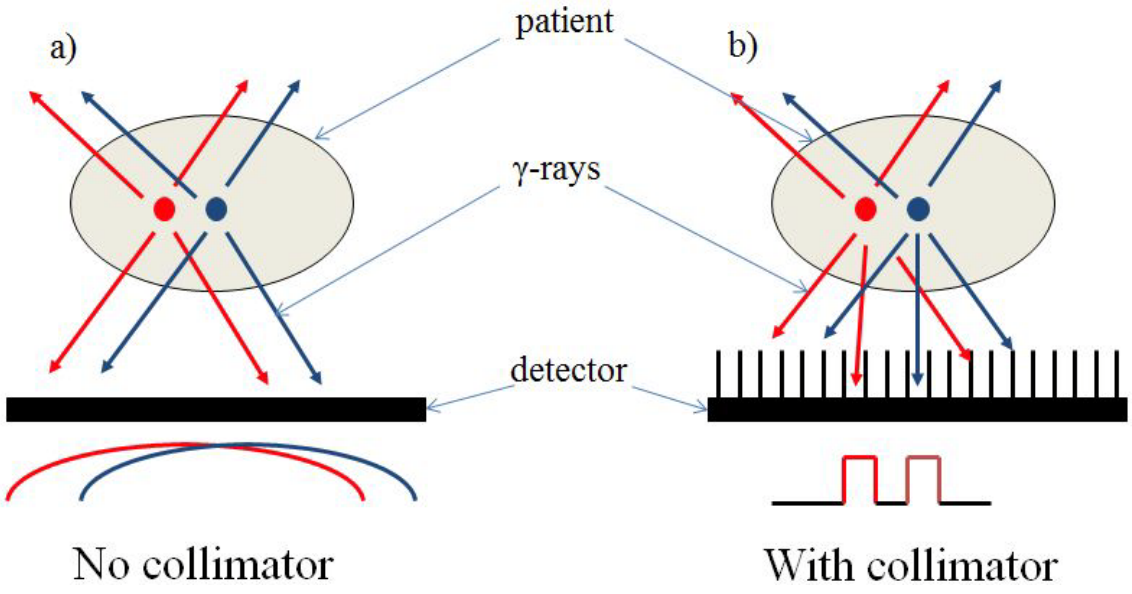

Figure 1.2: γ–ray detection in single-photon imaging. Concentrations of radioactive nuclides in the patient emit γ–rays: (a) shows that without a physical collimator, it is impossible to determine the origin of detected photons. Thus it is impossible to form an image. (b) shows that with a collimator, only photons travelling close to a specific direction are detected. Although far fewer photons are detected, a projection image can be produced.

PET, on the other hand, takes advantage of the back-to-back emission of annihilation photons to eliminate the need for a conventional collimator. A schematic of PET imaging is shown in Figure 1.3. With detectors on opposite sides of the object to be imaged, it is possible to detect both γ-rays from the same annihilation. If both annihilation photons interact with detectors, the electronic circuit within the scanner identifies interactions occurring at nearly the same time, a process called, annihilation coincidence detection (ACD). ACD works by monitoring the time at which γ-rays are detected; if they are from the same annihilation, they should be detected almost simultaneously. This is referred to as a *coincidence* and the system records a coincidence event and identifies it as being on a line of response (LOR) i.e. the line connecting the two detecors. The detection of one photon in one detector opens a timing window in the coincidence circuit. This window remains open for ~10 nanoseconds for whole body systems and for advanced systems this time window is 5 nanoseconds [11, 12]. The detection of the second photon, in the other detector, during this time frame completes the process, and an annihilation event has been

identified (Figure 1.3). Since the γ-rays are emitted 180° apart, the LOR passes through the origin of the annihilation. When multiple LORs are recorded as more γ-rays are detected, the set of LORs can be used to localize the site of annihilation. This method of using arrival times of the photons to locate the origin of annihilation is called *electronic collimation* and is one from many of the key benefits of PET over single-photon imaging. It is superior to the physical collimators used in single-photon imaging because a larger fraction of the emitted γ-rays can be detected. Also, spatial resolution does not degrade dramatically as the distance from the detector increases, as opposed to when collimation is used to form projection images.

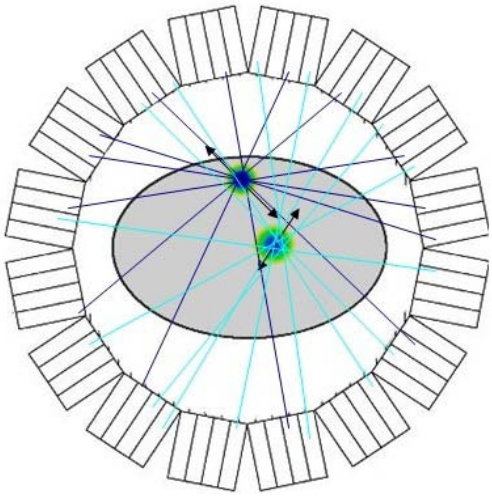

Figure 1.3: In PET imaging, coincidence event is used instead of a collimator in SPECT. γ-rays from the same annihilation can be determined by annihilation coincidence detection (ACD) and forms lines of response (LOR). With many LORs, the origin of annihilation can be determined.

Another advantage of PET is the high-energy γ-rays involved during the annihilation process. Compared to lower energy photons in some single-photon studies, (60-140 keV) [13, 14], these high-energy γ-rays have a higher chance of escaping the body of the patient without undergoing any interactions with the patient. Furthermore, all positron emissions, regardless of the type of radionuclide, will eventually result in the emission of 511 keV annihilation photons. PET scanners, therefore, only need to be optimized for one photon energy. But this puts limitation on using multiple traces imaging.

1.3.1.3. Positron range

Positron emission brings significant benefits to medical imaging applications, but the physics of positron emission also puts limits on the achievable spatial resolution of PET images. The first drawback is caused by the *positron range*, which is defined as the distance between the location of positron emission and the location of the subsequent annihilation (Figure 1.4). When a positron is emitted from the nucleus, it must lose kinetic energy by interacting with other electrons before coming to a stop to form a positronium. The path travelled by a positron is tortuous because of the frequent direction-changing interactions with electrons and matter. The positron range is therefore shorter than the total path length. The positron range is affected by the initial kinetic energy of the positron; radioactive decays that involve a larger change in energy will result in positrons with a higher initial kinetic energy and a larger average range. Table 1.3 show the average range traveled by positron from different radiotracers used in PET imaging. Since the LORs resulting from the detection of annihilation photons only identify locations of annihilations and not the actual location of positron emission, positron range acts to degrade spatial resolution. The positional error caused by positron range is the perpendicular distance from the annihilation location to the LOR.

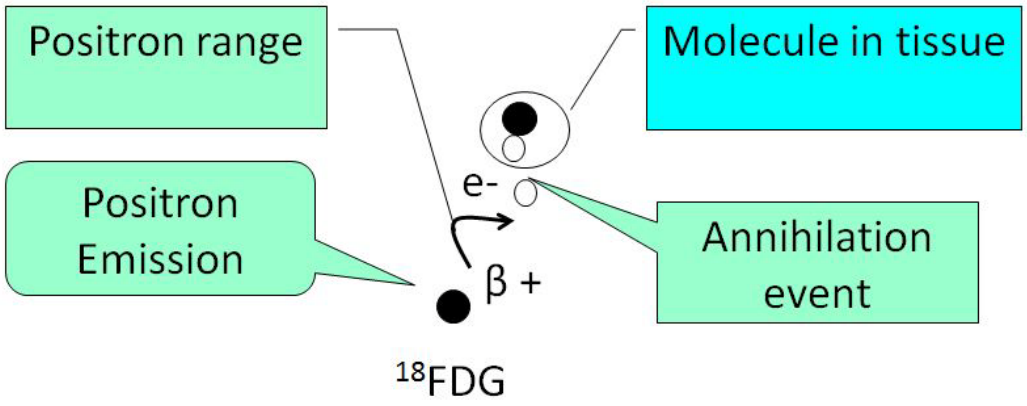

Figure 1.4: When a positron is emitted as a result of radioactive decay, in this example the decay of FDG, it travels a tortuous path because of the frequent interactions with electrons in the surrounding material. It finally comes to a stop and annihilates with an electron. The distance between this location and the initial positron emission is the positron range. The contribution to spatial resolution by the positron range is the perpendicular distance between the positron emission and the path of annihilation photons.

Table 1.3. The average range traveled by positron from different radiotracers used in PET imaging [17].

Isotope	Half-life	b^+ fraction	Max. Energy	Range(mm)
C–11	20.4 mins	0.99	0.96 MeV	0.4 mm
N–13	9.96 mins	1.00	1.20 MeV	0.7 mm
O–15	123 secs	1.00	1.74 MeV	1.1 mm
F–18	110 mins	0.97	0.63 MeV	0.3 mm
Cu–62	9.74 mins	0.98	2.93 MeV	2.7 mm
Cu-64	12.7 hours	0.19	0.65 MeV	0.3 mm
Ga–68	68.3 mins	0.88	1.83 MeV	1.2 mm
Br-76	16.1 hours	1.00	1.90 MeV	1.2 mm
Rb–82	78 secs	0.96	3.15 MeV	2.8 mm
I–124	4.18 days	0.22	1.50 MeV	0.9 mm

1.3.1.4. Noncolinearity

Another drawback of positron emission results from the fact that a positron is not completely at rest when it forms a positronium atom with an electron; the net momentum is non-zero. In order to conserve momentum, the annihilation photons are emitted at angles slightly different from 180°. This effect, shown in Figure 1.5, is called *noncolinearity* and causes mispositioning of the LOR because PET reconstruction algorithms assume the annihilation photon emission to be 180°. Because of the small angles involved, the effect of noncolinearity is estimated by simple trigonometry, given by:

$$\Delta_{noncolinearity} = 0.0022D \,, \tag{1.7}$$

where D is the diameter of the PET detector ring. Note that the error increases linearly with the size of the detector rings, but is independent of the initial kinetic energy of the positron.

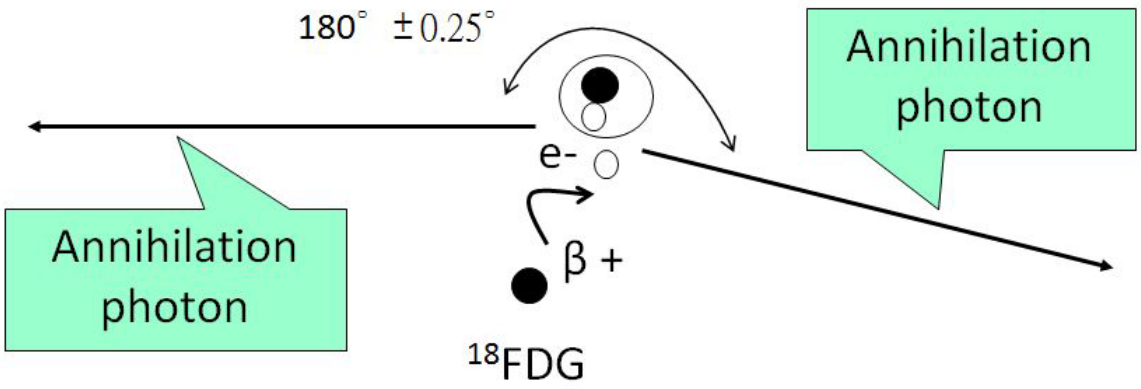

Figure 1.5: The non-zero momentum of the positronium causes the annihilation photons to be emitted at angles slightly different from 180° (The angle in the figure is exaggerated). The resulting LOR misses the site of annihilation.

1.3.2. γ-ray interactions

It is important to understand how γ-rays interact with an absorbing medium, so that the effects of scattering in the patient are understood and γ-ray detectors, and shielding can be properly designed. With the 511 keV γ-rays involved in PET imaging, the *photoelectric effect* and *Compton scattering* are the most important types of interactions.

1.3.2.1. Photoelectric effect

The photoelectric effect is shown in Figure 1.6, where a photon is completely absorbed by an atom. The energy of the incident photon is transferred to one of the orbital electrons, which is ejected from the atom as a *photoelectron* with energy given by:

$$E_{photoelectron} = E_{\gamma} - E_b \ , \qquad (1.8)$$

where $E_{photoelectron}$ is the energy of the photoelectron, E_{γ} is the energy of the incident photon (511 keV in PET), and E_b is the binding energy of the orbital electron. The photoelectron because it is a charged particle, interacts with other electrons in the absorbing medium and is absorbed in a short distance. The vacancy left in the atom by the photoelectron is filled by an electron from the outer shells, causing a *photon* to be emitted with energy equal to the difference in binding energies of the initial and final

shells of the electron. Since the energy of this photon is relatively low, in a detector it is also absorbed in a short range. The net effect is local deposition of the γ-ray energy.

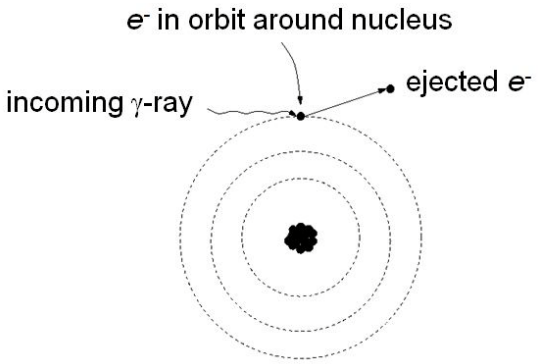

Figure 1.6: In the photoelectric effect, the incoming γ--ray is completely absorbed by the atom and the energy absorbed is used to eject an electron from the atom.

The probability of a photon undergoing photoelectric absorption per unit distance, τ, depends on photon energy and the atomic number of the absorbing medium; photons with lower energy are more likely to interact by photoelectric absorption, especially in materials with higher atomic numbers. The dependence of τ on Z and E_γ is given by:

$$\tau \propto \frac{Z^3}{E_\gamma^3} \; ; \tag{1.9}$$

1.3.2.2. Compton scatter

Another common way a photon interacts with an absorbing medium is by Compton scattering, shown in Figure 1.7. In this interaction, the photon interacts with a loosely bound electron and is deflected, or scattered, while depositing part of its energy to the electron. The electron is ejected from the atom as a *recoil electron*.

The energy transferred to the scattered photon is related to the scattering angle θ by [14]:

$$E_{scatter} = \frac{m_e c^2}{\frac{m_e c^2}{E_\gamma} + 1 - \cos\theta} \; , \tag{1.10}$$

where E_γ and $E_{scatter}$ are the energies of the incident and scattered photon, respectively, and $m_e c^2$ is the rest-mass energy of an electron. The remainder of the energy is transferred to the recoil electron. For 511 keV γ-rays in PET, (1.10) can be simplified to:

$$E_{scatter} = \frac{511}{2 - \cos\theta}, \tag{1.11}$$

Equation (1.11) indicates that the maximum amount of energy deposited by Compton scattering occurs when θ=180° (back scatter). In this case, 33% of the initial photon energy is scattered and 67% is absorbed. On the other hand, when θ =0°, no energy is lost and the incident photon continues on its original path. The probability of Compton scattering per unit distance, decreases gradually with increasing E_γ, and is proportional to density but relatively independent of Z [14].

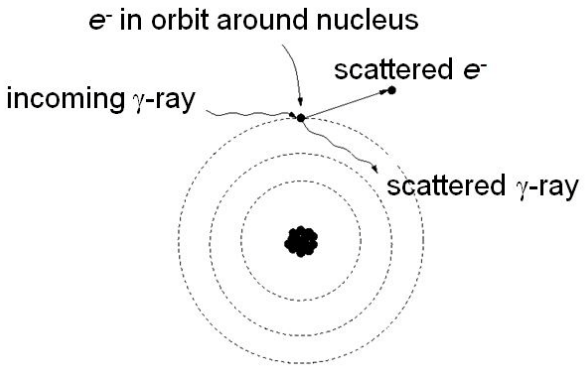

Figure 1.7: In Compton scattering, the energy of an incoming γ-ray is partially absorbed by the atom, ejecting an electron from the atom and scattering the photon.

1.3.2.3. γ-ray attenuation

When a 511 keV photon travels through a certain thickness of an absorbing medium, it may interact with the atoms by one of the two processes described above, or it may continue without any interaction. If a photon is absorbed or scattered in the absorbing medium, it is said to be *attenuated*. The number of *unattenuated* photons after a distance of l in an absorbing medium is given by:

$$I(l) = I(0)e^{-\mu l}, \tag{1.12}$$

where *I(l)* is the number of unattenuated photons after traveling a distance *l* and *I(0)* is the initial number of photons. μ is defined as the probability of interaction per unit distance travelled, and is called the *linear attenuation coefficient*. With the majority of interactions of a 511 keV photon being the photoelectric effect and Compton scattering,

$$\mu \approx \tau + \sigma; \tag{1.13}$$

1.3.3. Detector module

The component in a PET scanner that detects γ-rays is the *detector module*, or simply the *detector*. A detector must detect the γ-rays as efficiently as possible, since the statistical quality of the PET image increases with the number of γ-rays detected. Higher detection efficiency also means that a lower dose of radiopharmaceuticals may be used, or the imaging time may be decreased to reduce image blur due to patient motion and also to increase patient throughput. It is also important to locate where a γ-ray interacts within the detector in order to improve spatial resolution of the PET image by recording accurate LORs. To identify γ-rays coming from the same annihilation by ACD, a detector must have a good timing resolution, which is the ability to accurately determine the time when a γ-ray is detected. The better the timing resolution, the more effectively a PET detector can distinguish between *true coincidences* (two γ-rays from the same annihilation detected at the same time) from unwanted *random coincidence* (random, unrelated γ-rays detected at the same time by chance). Finally, a PET detector must determine the energy of the detected γ-ray. This is because a γ-ray that undergoes Compton scattering changes its direction and loses energy. If these γ-rays are not rejected, they will result in incorrect LORs being recorded. Therefore, it is necessary to identify and reject these unwanted γ-rays which can be identified based on the photon energy. The accuracy with which a detector can determine the γ-ray energy is called the *energy resolution* of a detector.

Detector modules in the majority of PET systems consist of a scintillation crystal and a photo detector (Figure 1.8). The scintillation crystal is responsible for interacting with γ-rays and converting the absorbed energy to visible light, while the photodetector detects the visible light and converts it to an electrical signal.

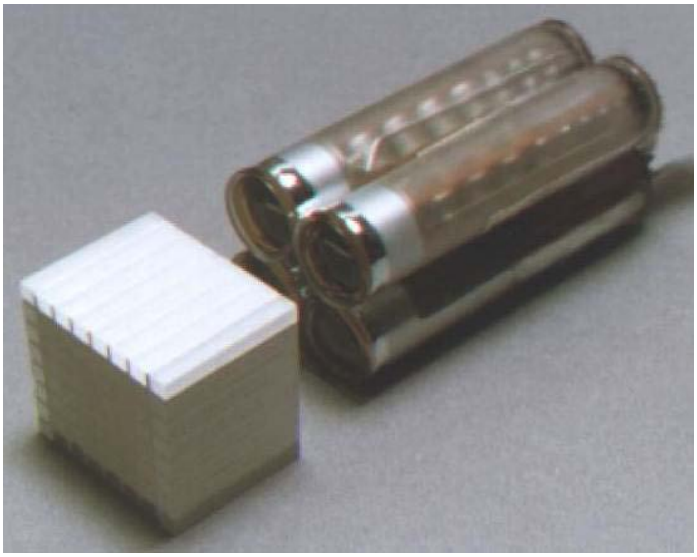

Figure 1.8: Shows detector module (separated for illustration purposes) for a conventional clinical PET system. It consists of a block of scintillator crystals and an array of photomultipliers (PMTs).

1.3.3.1. Scintillator

Scintillators used in PET imaging are transparent crystals that emit *scintillation photons* with wavelengths in the visible range in response to an interaction with a high energy γ-ray. The number of scintillation photons produced should be in proportion to the amount of energy transferred by the γ- ray to the scintillation crystal.

One of the most important characteristics of a scintillator is the stopping power. Ideally, a scintillator should absorb all incident γ-rays. A scintillator should have a high stopping power to minimize the thickness needed to interact with most of the γ-rays. More specifically, photoelectric absorption is preferable to Compton scattering in the scintillator. Typical scintillator thickness in commercial PET scanners is on the order of a few centimeters, and unfortunately, photoelectric effect accounts for less than half of the interactions. For example, BGO has a photoelectric fraction of 40% and has a linear attenuation coefficient of 0.96 cm^{-1} at 511 keV; a thickness of 2.4 cm is required to stop ~90% of the γ-rays. For LSO 2.6 cm of thickness is required to stop the same amount. Table 1.4 shows characteristics of different scintillators used in PET. The BGO crystal shows very good efficiency but long decay time and poor output. The better choice would

be LSO crystals with comparably good stopping power as well as higher light yield and shorter decay time. But LSO crystals is more expensive.

Table 1.4: The characteristics of different scintillator crystals used in PET

Scintillator	90% efficiency (cm)	Light output (photons/MeV)	Decay time (ns)
BGO	2.4	7,000	300
BaF_2	5.1	2,000	0.8
CsF	5.4	1,900	4
LSO, LYSO	2.6	25,000	42
$LaBr_3$	4.9	60,000	27

It is also important for a scintillator to have a high light output, commonly expressed as the number of scintillation photons emitted per unit energy deposited. Firstly, the magnitude of the light output of a scintillator is used to determine the energy of the absorbed γ-ray. Secondly, in light-sharing detector modules (to be discussed in Section 1.3.3.3), the relative number of photons detected by adjacent photodetectors is used to determine the location of the γ-ray interaction. Because the emission of scintillation photons is governed by Poisson statistics, the signal-to-noise ratio (SNR) of the light output is the square root of the average number of photons. Therefore, it is desirable to have a high light output for better SNR and a corresponding in better energy resolution. In the case of light-sharing detectors, a brighter output also means better spatial resolution.

The decay time is another important property; it affects the timing resolution and the time required to process an interaction. With a bright and fast light output, there will be less variation in determining the start of the signal, thus improving the timing resolution. Also, since less time is needed to collect the scintillation light, the detector will be ready to detect the next γ-ray sooner. And this will result to a shorter dead-time of the block detector. Finally, the optical coupling between the scintillator and the photodetector depends on their refractive indices; mismatching refractive indices will result a less efficient transmission of light.

1.3.3.2. Photodetector

The second part of a block detector is the photodetector, which is responsible for detecting scintillation photons and converting them into an electrical signal. A photodetector should convert the light photons emitted from the scintillation crystal into charge carriers efficiently to obtain the best estimate of the energy deposited by the γ-ray. This conversion is characterized by the *quantum efficiency* (QE) of the photodetector, which depends on the wavelength of the scintillation photons. QE is ratio of number of collected electrons on number of incident photons. Even with QE = 100% each detected scintillation photon initially creates only one ehp charge carrier, therefore a large internal gain is needed so that the electrical signal at the output will have a good SNR.

The electrical signal is also used to determine the time of the γ-ray interaction. The simplest way to do this is by monitoring when the output signal rises above a pre-determined threshold. To accurately perform this *time pick-off*, a signal with large amplitude and a fast *rise time*, defined as the time required for the signal to change from l0% to 90% of its maximum, is needed to minimize any electronic noise from the electronic circuits. A photodetector with minimal fluctuations in the time interval from the detection of a photon to the appearance of an output signal is also necessary. This fluctuation is expressed as the *transit-time spread* (TTS). Finally, in order for a detector to quickly recover from an interaction and become ready to detect the next γ-ray, the photodetector should have a short *charge-collection time* (CCT). The charge carriers generated by the photons should be collected quickly to avoid interfering with new charge carriers generated by the next burst of scintillation light.

PMT is a vacuum tube where a photocathode is located on the inside surface of the glass entrance window at the end of the tube facing the light source. When photons pass through the entrance window, they interact with the photocathode to produce photoelectrons with a QE for blue light typically around 25% [14, p.102]. This means that on average, 25% of the incident photons are successful in producing primary photoelectrons. The electric field inside the PMT accelerates these photoelectrons towards a positively-biased dynode. With enough energy gained from the acceleration

through the electric field, each photoelectron striking the dynode will cause a number of secondary electrons to be released from the coating material of the dynode. These electrons then accelerate towards the next, even more positively-biased dynode and the process continues until the electrons reach the anode and are collected. With for example 3 electrons gained in each dynode and 10 stages, PMTs enjoy a large gain up to 10^6 (Figure 1.9). The typical rise time and TTS are on the order of a nanosecond, whereas the CCT is about ten times slower.

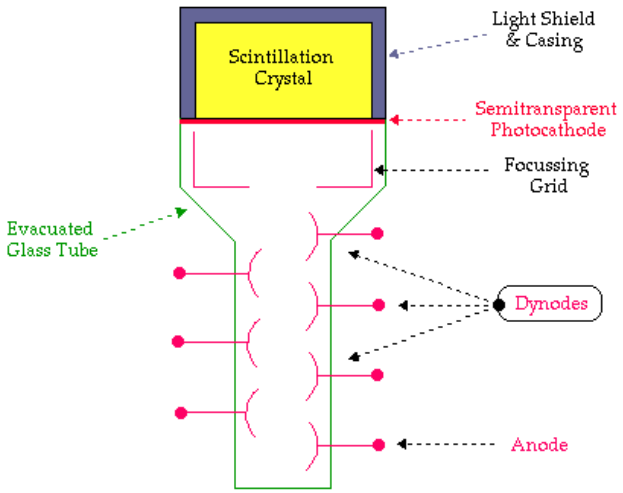

Figure 1.9: Schematic of a photomultiplier tube with a scintillation crystal coupled.

1.3.3.3. Block detector

The most straight-forward way to construct a detector module is to use one PMT to detect the light from one scintillator like in Figure 1.9. However, this implies there will be as many PMTs as detector pixels. While this was acceptable for first generation PET scanners, the high cost of PMTs and their bulkiness make this design impractical to achieve today's scanners with 10,000 detector pixels. The block detector was designed to address this problem [15]. Using a light-sharing readout method, the size of the scintillator pixels can be made smaller, the pixels can be packed more tightly together, and the number of PMTs required is also reduced.

Figure 1.10 shows a block of crystal scintillator partially cut into many smaller segments, which are read using only four PMTs. The depths of the cuts are designed such that when a photon is incident on one of the crystals, the resultant light is shared by all 4 PMTs. Light distribution on the four PMTs varies according to the segment which interacted with γ-ray. When light photons are absorbed all four PMTs produce a signal. Anger logic is used to calculate the exact pixel where the γ-ray interacted with the crystal:

$$X = \left(\frac{A + B - C - D}{A + B + C + D}\right)$$
$$Y = \left(\frac{A + D - B - C}{A + B + C + D}\right) \quad , \tag{1.14}$$

where *A*, *B, C* and *D* are the fractional amounts of light detected by each PMT (numbering shown in Figure 1.10). Typical block detectors in today's commercial PET scanners have scintillators that are cut into 64 scintillator pixels with widths of 3-5 mm and a length of 20-30 mm [16].

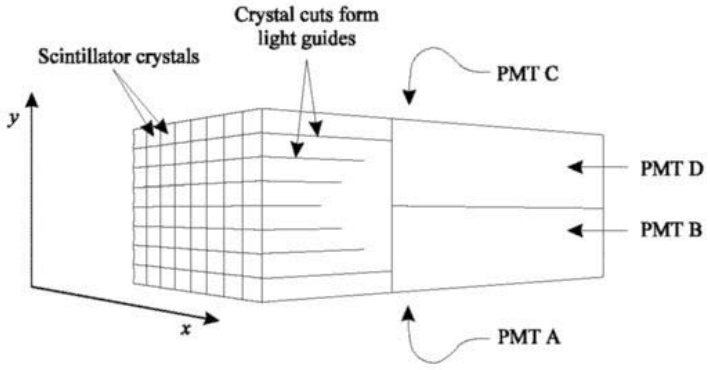

Figure 1.10: Schematic representation of conventional PET block detector, four PMTs is optically coupled to the back of a scintillator.

1.3.4. Detector ring for whole body PET

In a PET scanner, a large number of individual detectors are arranged in a circular array to form a *detector ring* in order to detect back-to-back annihilation photons emitted from the patient. Each detector is capable of performing ACD with multiple detectors on the opposite side of the detector ring, and many pairs of annihilation-photon pairs can be

detected simultaneously. The direction along the axis of the detector ring is the *axial* direction, whereas the plane perpendicular to this axis is the *transaxial* plane. For a whole-body PET scanner, the diameter of the detector ring is typically around 80 cm wide. To increase sensitivity to γ-rays, several detector rings are usually put together to increase the solid angle coverage of the detectors. The total axial length is typically around 15 cm [16].

1.3.4.1. γ-ray detection efficiency

The system efficiency is determined by the probability of detecting a coincidence γ-rays interacting with the scintillator. The γ-ray detection efficiency of a PET scanner is determined by the *geometric efficiency*, the *detector efficiency* and *packing*. The overall γ-ray detection efficiency is:

$$\eta_{\gamma} = \eta_{geo}\eta^{2}_{\det ector}\eta_{packing} \ ; \tag{1.15}$$

Detectors in whole-body PET scanners are ussually arranged in a circular ring instead of geometries with better solid angle coverage of the patient, such as a long cylinder or a sphere, because such configurations require too many detectors, making the material cost of the scanner prohibitively high. As a compromise, γ-ray detection efficiency is sacrificed. For a ring geometry, geometric efficiency (at the center of the ring), η_{geo}, is given by [17]

$$\eta_{geo} = \sin[\tan^{-1}(\frac{A}{D})], \tag{1.16}$$

where A is the axial length of the detectors and D is the diameter of the detector ring. The first component depends on the stopping power of the scintillator and is given by

$$\eta_{\det ector} = (1 - e^{-\mu d}) \ , \tag{1.17}$$

where μ is the linear attenuation coefficient, and d is the thickness of the scintillator. Since both of the annihilation photons must be detected, the detector efficiency, η, is squared when the overall γ-ray detection efficiency is calculated. The second component is determined by the fraction of active-area in the detector. This *packing fraction* is simply

$$\eta_{packing} = \frac{active\_area}{active\_area + inactive\_gaps}, \tag{1.18}$$

The detector efficiency, η_γ, in clinical whole body PET is <6% [18].

1.3.4.2. Spatial resolution

A fundamental limit on the spatial resolution of a PET scanner is coming from the physics effects of positron emission, namely *positron range* and *noncolinearity*. However the major contributor to *spatial resolution* degradation is the detector. Firstly, the detector resolution is affected by the pixel size of a crystal scintillator. This resolution is described by the *coincidence response function*, and is measured by moving a point source of radiation between two detectors as shown in Figure 1.11. At each horizontal position, the fraction of annihilation events detectable by the detector pair (assuming the detectors have 100% stopping power) is recorded. When this is measured in the half distance between a detector pair with a pixel width of *d*, the coincidence response function has a triangular shape with a full width half maximum (FWHM) of ~ *d/2*. The effect of pixel size for a whole body PET scanner is shown on Figure 1.12. Smaller detectors yield better resolution and better sampling.

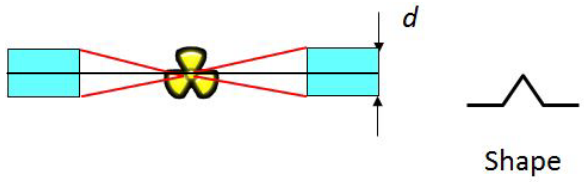

Figure 1.11: The contribution to spatial resolution by the pixel size is described by the coincidence response function. The coincidence response function records the number of annihilation events detected as a function of distance. At the middle of the two detectors, the function has a triangular shape.

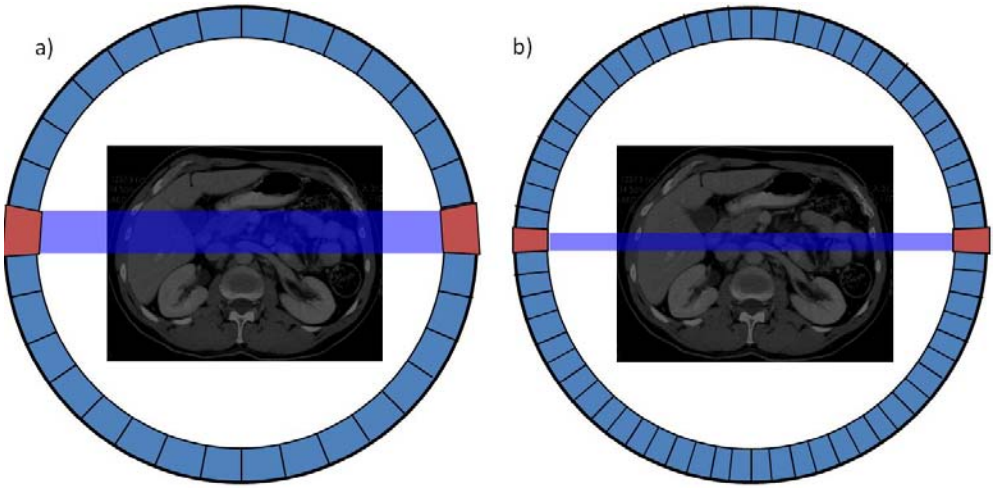

Figure 1.12: The effect of pixel size in whole body PET systems using ring detectors. a) pixel size is larger which results in bad spatial resolution. b) pixel size is smaller so this improves spatial resolution.

Secondly, the fact that the crystal scintillators do not have 100% stopping power also contributes to spatial resolution. Recall that the stopping power is related to the linear attenuation coefficient of the scintillation crystal and its thickness. As shown in Figure 1.13, when incident γ-rays strike the detector at an angle, the effective thickness of the scintillator is changed, resulting in a different probability of the γ-ray escaping the detector without any interaction.

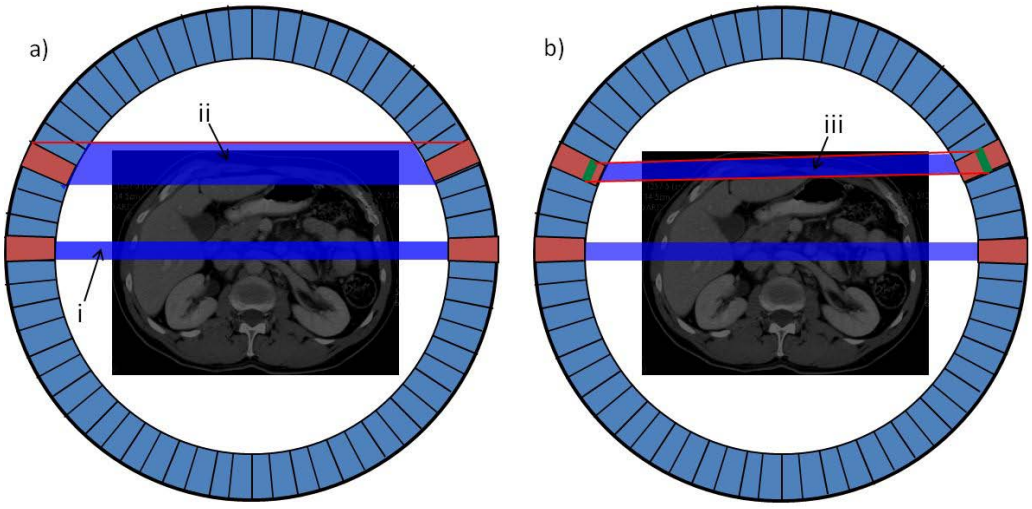

Figure 1.13: The effective length of scintillation crystal depends on the angle of the incident photon. Usually, it is assumed that the incident photon strikes the scintillator normally (i). However, as the incident angle changes, the effective length of the spatial resolution can become longer (ii) or shorter and tilted (iii).

Consider γ-rays emitted at the off-center locations in a ring detector, shown in Figure 1.13. These γ-rays may strike the detectors at some angle, and it is possible for them to interact with any one of the two detectors in its path. As γ-ray not necessarily absorbed by the first scintillation crystal it interacted. As the energy of the γ-ray is high the photon may interact only with the second scintillation crystal. Without knowledge of exactly where inside the detector an interaction takes place, an assumption has to be made and the resulting LOR may not overlap with the origin of the annihilation. This is called the parallax effect and is a direct result of the lack of *depth-of-interaction* (DOI) information from the detectors. It is due to the non-uniform spatial resolution of PET images across the field of view (FOV), and can degrade spatial resolution over a large fraction of a PET scanner's FOV [19]. Due to this limitations clinical PET systems, at best, have a resolution of 6 to 8 mm [16].

1.4. Positron Emission Mammography

A significant role in cancer diagnosis has to be dedicated to Positron Emission Mammography (PEM). Worldwide, 7% of all deaths from cancer are due to breast cancer. In Canada, more than 20 000 Canadian women are diagnosed with breast cancer each year. This is the most prevalent cancer in women, accounting for 27.6% of all women cancer cases [20]. One in three women with breast cancer will die as a result of this disease [20]. The crucial step in reducing the rate of mortality from breast cancer is to detect it in its early stages before the disease progresses ideally when primary tumor does not exceed 1 mm in size. In this case the disease is captured at its non-invasive state resulting in much better prognosis [21].

Conventionally, x-ray mammograms were used to diagnose breast cancer. However, functional imaging provides a more effective method for detecting suspicious breast lesions compared to x-ray mammography, due to the use of tracer-avid radiopharmaceuticals. In addition, some PET radiopharmaceuticals, like FDG, demonstrate good breast tumor targeting capabilities. Figure 1.14 compares a regular mammogram to a conventional PEM scan. As it is seen from the figure, cancer is obvious on the PEM scan but not on the mammogram.

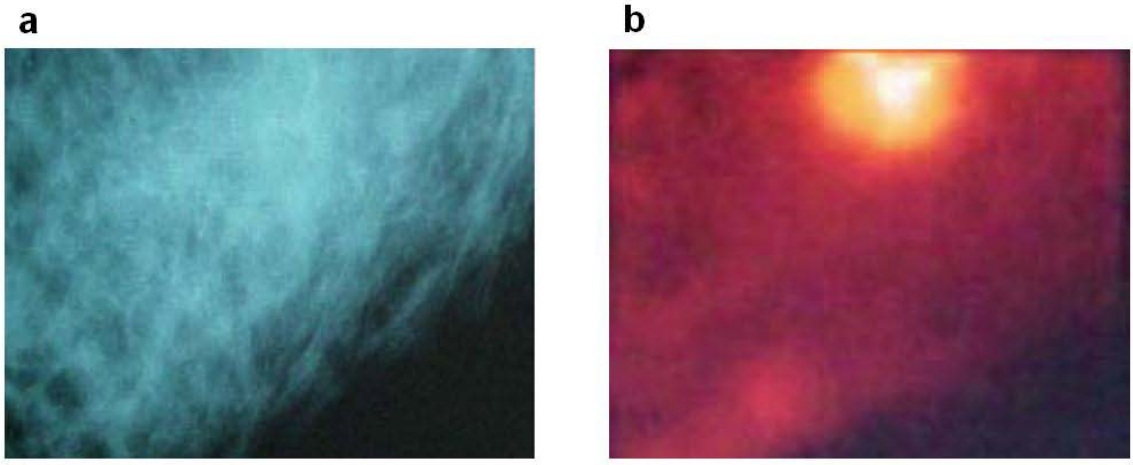

Figure 1.14: Scan of the same breast containing cancer tumor. (a) the x-ray mammogram does not show the cancer. (b) PEM scan clearly identifies the location of tumor as the bright yellow sphere.

However, current whole body PET scanners do not meet the performance levels required for early breast cancer diagnosis. They must possess a spatial resolution of ~1 mm while they can only achieve 6-8 mm in the current state of the technology [16]. To overcome this limitation, Thompson and Weinberg [22] designed a scanner dedicated to the early detection of breast cancer that has a more optimal geometry, in order to achieve higher detector efficiency and resolution. Furthermore, positron emission mammography scanners use dual-headed opposing planar coincidence detectors between which a breast can be immobilized with mild compression. In light of this, using dedicated detectors that are very close to or in contact with the breast being imaged is extremely advantageous in many ways. First, these systems have greater geometric efficiency due to the large solid angle subtended by the detectors. This results in a significant increase in detection efficiency. Moreover, the compression used by most systems reduces attenuation, which also increases the detection efficiency. Also, the small distance between the detectors reduces blurring due to noncolinearity to less than 0.25 mm - much smaller than a pixel. Finally, employing small crystals in this detector configuration further improves the resolution over whole-body PET scanners (< 2.5 mm (new design) vs. > 6 mm FWHM (WB)).

Although these characteristics allow PEM to detect breast cancer when it is smaller and therefor earlier in its development than is possible with whole body PET scanners, PEM has many other advantages as well, such as high specificity. Other benefits of PEM include image-guided biopsies as well as correlating x-ray mammograms to PEM images by incorporating both imaging devices into one system [23].

1.5. New detector designs

The original PET detector design has some issues that need to be addressed. For instance, there are some inherent limitations with the block detector. Firstly, it is only able to locate a γ-ray interaction two-dimensionally; systems made with block detectors suffer from parallax error because of the lack of DOl capability. This problem leads to PET images with non-uniform spatial resolution, where the spatial resolution degrades as the distance from the center of the FOV increases. Secondly, the low QE and non-uniform sensitivity of the PMTs limit the resolving power of Anger logic and puts a limit on the minimum size of the crystal pixels. In other words, both the parallax problem and the shortcomings of PMTs prevent the use of longer and narrower crystal pixels for higher sensitivity and better spatial resolution. Another limitation is that all four PMTs are involved in light collection whenever a γ-ray interacts with the block detector and the whole module is paralyzed. Consequently, the dead time (the time when the detector is unavailable for further γ-ray detection while the outputs of the PMTs are analyzed) affects the area of the entire detector module. The effective dead time is proportional to the size of the block detector and limits the maximum count rate (γ-ray detection rate) of the block detector. Although commercial PET scanners still rely on the detector block, a number of new detector module designs have been proposed to address the aforementioned shortcomings.

1.5.1. PEM detector modules

To detect breast cancer in its early stages with PEM, we need to design detector modules with higher spatial resolution. The approach taken to do so consist of designing PEM photodetectors with solid state photoconductors which will replace the bulky and

inefficient PMTs. Using solid state photosensors will allow the construction of much thinner detector heads, which will allow them to be positioned closer to the breast. This results in an increase in collection efficiency, leading to a much better image. The concept system design is shown on Figure 1.15.

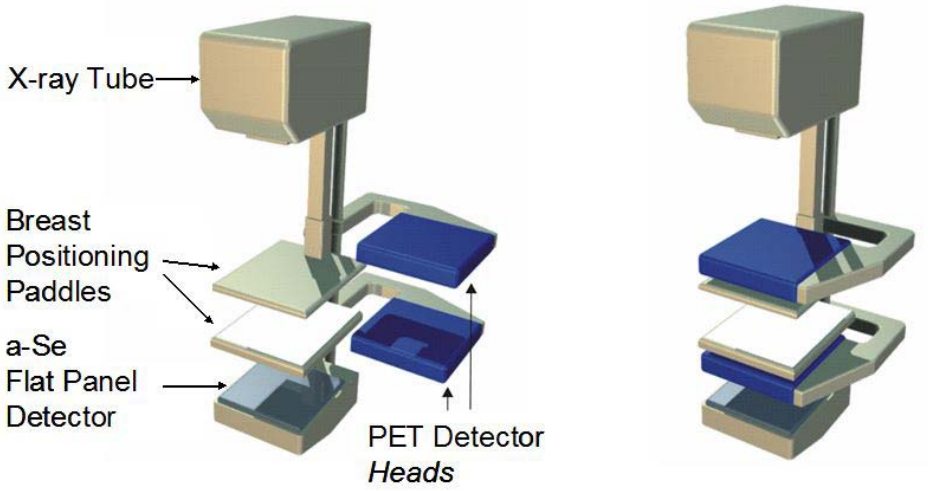

Figure 1.15: Two compact PET Detector Heads are mounted on rotating arms that allows adjustable detector heads separation and positioning. Left: x-ray mammography setup: PET detectors are swiveled out of the way. Right: Functional imaging setup: PET detectors are aligned with the breast-positioning paddles.

Such design can be improved by using large area photodector. This is discussed in Section 1.5.2 .

1.6. Amorphous selenium

A compact photodetector design based on solid state rather than electro-optical principles is crucial to the development of practical dual detector modules. Other than their compactness, these solid-state devices have additional benefits over PMTs. They are rugged devices and have a higher QE for scintillation light than PMTs (98% for a-Se comparably to 25% for PMTs, for blue light). Furthermore, using only solid-state photodetectors, the photo detector module is insensitive to magnetic fields, opening the possibility of PET/MRI systems [24, 25]. However, Si PDs have no internal gain and Si APDs only have a moderate gain on the order of 100. As a result, electronic amplifiers

must be used to provide further gain, but the electronic noise associated with these amplifiers presents another source of noise.

Amorphous selenium (a-Se), on the other hand, has been shown to produce a large gain from avalanche multiplication with low dark current. As a solid state material, a-Se shares many of the benefits that crystalline Si provides, such as compactness and insensitivity to magnetic fields. In addition, a-Se has superior QE at the wavelengths important to PET. Also, it is a low cost material that can be evaporated onto a large-area making a-Se an attractive alternative to crystalline Si devices. We therefore propose using a-Se layers as the photodetectors in the new photodetector module.

Chapter 2 Fast a-Se photodetector with avalanche gain for application in PET

2.1.Introduction

To date, a-Se remains the only amorphous semiconductor in which there is clear evidence that the primary charge carriers (holes) can acquire enough energy from the applied field to initiate impact ionization and secondary charge creation [26,27,28]. Impact ionization at high fields results in avalanche multiplication, *M*, which depends exponentially on the photoconductor layer thickness [29,30]. Experiments on impact ionization of holes in a-Se indicate that avalanche is initiated at electric fields exceeding a certain avalanche multiplication threshold, F_{th}. The latter is about 70 V μm^{-1} for a-Se layers thicker than 15 μm; F_{th} depends slightly on the a-Se thickness. Thus far, a maximum avalanche gain of 10^3 has been demonstrated for a 30 μm thick a-Se layer at a field of 92 V μm^{-1} [1]. The avalanche gain capability of a-Se photoconductors potentially provides practical solutions to a number of important applications in the field of medical imaging detectors, in as much as it promises to increase a-Se's light to charge conversion efficiency and lead to a-Se detectors that are effectively quantum noise limited in operation. A further often overlooked advantage of avalanche multiplication is to increase the dynamic range of a system by permitting the maximum signal capacity to be adjusted by changing the effective multiplication gain. There have been a number of recent studies by Rowlands and coworkers that have examined the use of avalanche in a-Se for medical imaging applications [31,32,33,34,35,36] as well as in protein crystallography [37,38]. The combination of high multiplication gain with high optical quantum efficiency and low dark current makes avalanche a-Se photosensors an alternative to photomultiplier tubes for a variety of optical and medical imaging applications, *e.g.* Positron Emission Tomography (PET) [39,40,41].

2.2. Background

We need to understand the important characteristics of a photodetector in a detector module before we can define the required properties of a-Se. We start by reviewing the

requirements of a detector module. Moses *et al.* summarized the requirements of the detector module in approximate order of importance. They are:

1. High detector efficiency (> 85% per 511 keV photon),
2. High spatial resolution (< 5 mm FWHM),
3. low cost (< \$93/cm^2),
4. low effective dead time (< 26 μs•cm^2),
5. good timing resolution (< 5 ns), and
6. good energy resolution (< 100 keV FWHM).

From these requirements of the detector module, we can identify the related characteristics of a PET photo detector.

1. *Detector efficiency* - detector efficiency is, defined as the probability that a γ-ray striking the detector module is absorbed. It is affected by (1) the thickness of the scintillator and (2) the packing fraction of the detector module. To maximize detector efficiency, the dead space between adjacent detector modules must be minimized. A-Se can be evaporated into a large-area, thin layer with a fill factor of nearly 100%. This is in contrast to PMTs, which have large inactive gaps between active areas. The absence of inactive gaps makes the a-Se layer an excellent photo detector for maximizing packing fraction.

2. *Spatial resolution* - The scintillator is the determining factor in the spatial resolution achievable by a detector module. There is a lower limit to the size of scintillator pixels because (1) having more pixels per unit area increases the dead space between adjacent pixels, and (2) small pixels increase the probability that energy from a γ-ray is deposited over several pixels by Compton scattering, resulting in a loss of counts. In a-Se, individual pixel elements can be made as small as the underlying readout pixels. A-Se based flat panel x-ray detectors using activematrix thin film transistors (TFT), readout with pixel dimensions as small as 80 x 80 μm and are already available. Therefore, a-Se can meet the spatial resolution requirements of a PET photo detector.

3. *Cost* - Two of the most costly components in a PET scanner are the scintillators and the photodetectors. Therefore, minimizing the cost of these components is crucial in making PET more cost-effective and more widely available. The cost of an a-Se photodetector is expected to be lower than that of PMTs and Si APDs; the a-Se layer is a

simple structure with no doping or any complicated components. A large area a-Se layer can be prepared by a low temperature evaporation method. This makes a-Se an attractive choice, especially for detector modules where photodetectors are needed on both sides of the scintillator for DOl capabilities.

4. *Effective dead time* - The effective dead time is the product of (1) detector dead time and (2) the detector area affected by the dead time. Therefore, both must be minimized to reduce the effective dead time. The a-Se photodetector module is superior to the block detector since dead time only affects the area of one scintillator pixel in a photodetector module, whereas it affects the entire area covered by the detector module in light-sharing detector modules such as the block detector. To minimize dead time, the scintillator should have a fast response, and the CCT in a photo detector should be short. Charge carriers in a-Se have a lower mobility than in Si, which may imply a longer CCT. But it is shorter than the regular decay time of conventional scintillation crystals used in PET.

5. *Timing Resolution* - The time between the absorption of a γ-ray and the generation of an electrical pulse should ideally be constant in order for the detector module to produce accurate timing information. However, this time delay fluctuates because of (1) randomness in the emission of light by the scintillator after γ-ray absorption, (2) differences in transit time within the photodetector, and (3) the uncertainty in the time pick-off due to electronic noise.

The fluctuation in transit time is expressed as the TTS. In a PMT, the TTS arises primarily from the different photoelectron path lengths from the photocathode to the first dynode, which depend on the shape of the photocathode, design of the focusing electrodes, applied voltage, and the location and angle of the photoelectron. In a-Se, however, visible photons are absorbed very close to the surface, and the difference in distance the photogenerated charge carriers must travel before reaching the cathode is negligible. Therefore, the TTS of an a-Se layer is expected to be short compared to PMTs.

Electronic and other sources of noise cannot be completely eliminated from the photo detector signal and contribute to the uncertainty in time pick-off by subsequent pulse

processing electronics. A fast rise-time is desired to minimize this time jitter. To estimate the rise time achievable by an a-Se layer, the mechanism of photo current generation must first be understood.

6. *Energy Resolution* - The energy of γ-rays is reduced if they undergo Compton scattering in the patient. It is desirable to identify and reject these scattered γ-rays because they contribute to noise in the final PET image. Good energy resolution is therefore desirable for rejecting scattered γ-rays. Energy resolution also affects depth resolution in the dual photodetector module, since DOl information is obtained by the ratio of the signals of the two photo detectors on the opposite ends of a scintillator. Energy resolution depends on (1) the energy resolution of the scintillator, (2) the QE of the photodetector, (3) fluctuations in the internal gain of the photo detector, and (4) electronic noise in the detector and subsequent signal processing electronics.

The QE of a-Se is higher than that of PMTs and Si APDs. Using the Onsager theory with published results, the QE of a-Se is as high as 98% for 420 nm at 100 V/μm. The superior QE implies that the a-Se photodetector is more efficient in detecting scintillation photons. It has also been shown that a-Se exhibits large avalanche gain in high electric fields, a desirable quality since a large signal from the photodetector can minimize the negative effects of subsequent electronic noise, or in other words, achieve higher SNR.

2.3. a-Se sample preparation

Three different types of solid-state a-Se detector structures were prepared based on the HARP target used in a vacuum tube device:

Type 1 structure: *standard* avalanche a-Se phototarget of High-gain Avalanche Rushing Photoconductor (HARP) tube with 0.8 mm^2 gold contacts. In HARP the a-Se photoconductive layer is sandwiched between specially designed blocking layers to prevent injection of holes and electrons from the positive and negative contacts respectively. More details about HARP blocking structure in Section 2.3.1.

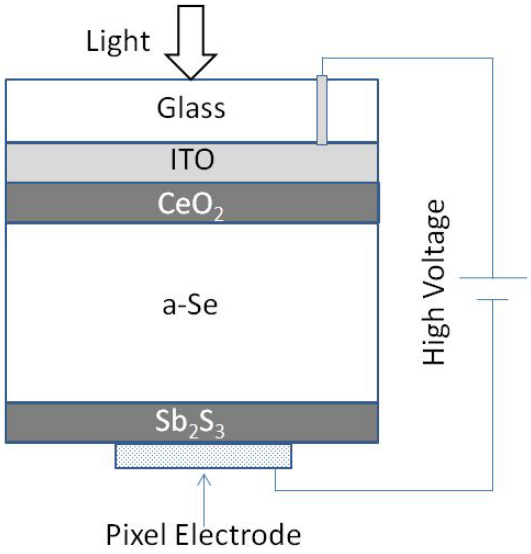

Figure 2.1: Schematic picture of a-Se structures under investigation: a-Se pixelated HARP blocking structure.

Type 2 structure: *modified* HARP phototarget in which a 1 μm thick RIL (using CA) was spin-coated prior to the deposition of a 0.8 mm^2 gold contact.

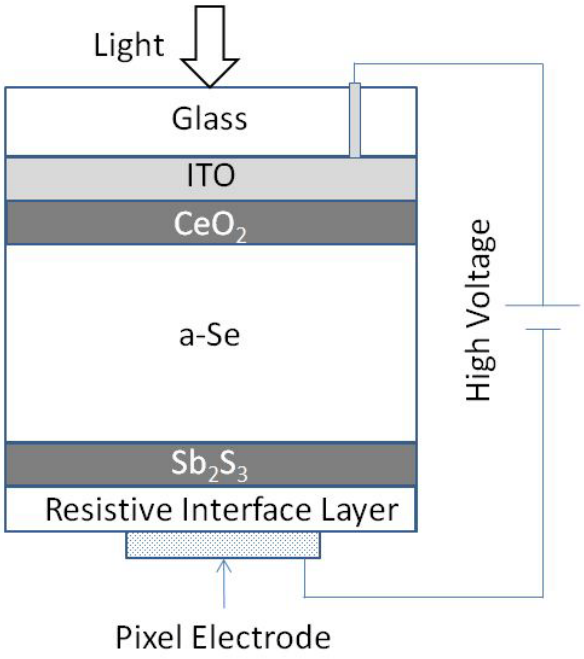

Figure 2.2: Schematic picture of a-Se structures under investigation: a-Se pixelated HARP blocking structure with Resistive interface Layer between a-Se and metal electrode.

Type 3*: no electron blocking layer* HARP phototarget. Type 3 is similar to Type 2 except that the electron blocking layer was not used and RIL was spin coated directly on the a-Se surface followed by contact deposition. The contact size was 2 mm in diameter for dark current measurements.

2.3.1. The HARP phototarget

Practical a-Se avalanche image sensors, called High-gain Avalanche Rushing Photoconductors (HARP), have been developed for broadcasting devices and exhibit a high multiplication gain ($g_{AV} > 200$ for $d = 15$ μm and $g_{AV} > 10^3$ for $d = 30$ μm) which provides ultra-high sensitivity and allows for functionality in extremely low light conditions [42,43,44]. Furthermore, HARP has two other remarkable features, high quantum efficiency (~ 95% for blue light) and low dark current [45,46]. The latter was made possible by the development of a special blocking structure that effectively suppresses charge injection from electrodes, even at the high electric field needed for avalanche [46,47].

The application of a high electric field to an a-Se photoconductor that would generate avalanche multiplication required the development of a special multilayer photoconductor structure; the goal was to use these structures in TV video tubes [48]. The a-Se based photoconductive target with avalanche gain is called a HARP, an acronym for High-gain Avalanche Rushing Photoconductor structure. The photoconductive a-Se layer is confined between specially designed blocking layers which almost completely block charge injection at high fields [49]: a thin layer of CeO_2 (~20 nm) on the front side (light receiving side) of the a-Se layer and Sb_2S_3 (~500 nm) on the back side, which receives the electron beam. Figure 2.3 shows the typical structure of a HARP. The CeO_2 and Sb_2S_3 layers serve as blocking layers for holes and electrons, respectively. The blocking mechanisms in these two layers are different from each other. CeO_2 is an *n*-type wide band gap material (E_g of 3.4 eV, E_F about 0.5 eV below E_c) and prevents the injection of holes from the anode by forming a high potential barrier to holes; electrons can drift freely through the CeO_2/a-Se interface. The Sb_2S_3 layer on the other hand has a band gap slightly narrower than that of a-Se, but it contains a large

number of deep electron traps which, when filled, form a negative space-charge barrier, thus stopping the injection of electrons from the cathode; at the same time holes can flow freely through the a-Se-/Sb_2S_3 interface. The HARP target was designed to be used in a vacuum device, that is, in the TV video tube (a TV pick-up tube). These tubes have been called *Harpicons*.

A-Se HARP structures have been developed by NHK in Japan as photoconductive targets of broadcast video cameras and are now used routinely for electronic news gathering in HDTV, *i.e.*, operation at low light conditions [50]. For use in optical imaging, a-Se HARP structure is deposited on a glass substrate covered with an ITO (indium tin oxide) coating, which serves as a transparent anode. The back of the a-Se HARP structure is free, that is, it has no physical electrode, which allows it to form a latent charge image. A scanning electron beam serves as a virtual cathode, biasing the free surface (see Figure 2.3). Light photons incident on the front a -Se surface through a positively biased ITO electrode are absorbed and create EHPs. The freed holes drift to the free surface of the a-Se layer and if the electric field exceeds F_{th}, the drifting holes undergo avalanche multiplication. The holes accumulate as a latent charge image at the free surface in an amount proportional to the incident light intensity. An electron beam scans the free surface, completing the circuit, and enabling the accumulated positive charge to be sensed by the ITO electrode as a current. There have been many examples on the uses of Harpicons in low-light level applications in which they outperform all standard imaging chips; Figure 2.4 has a sample image from a real-time movie of a rainbow observed under moonlight at night.

An a-Se photodetector is shown in Figure 2.5. Photons in the visible range enter the a-Se layer from the transparent anode, with most being absorbed within the first micron of the a-Se, creating electron-hole pairs (EHPs). Due to the direction of the applied electric field, F, electrons are collected almost immediately by the anode and contribute little to the signal. The holes drift towards the negatively biased metal electrode on the other side of the layer, inducing an electrical current as the charges move as described by Ramo's Theorem.

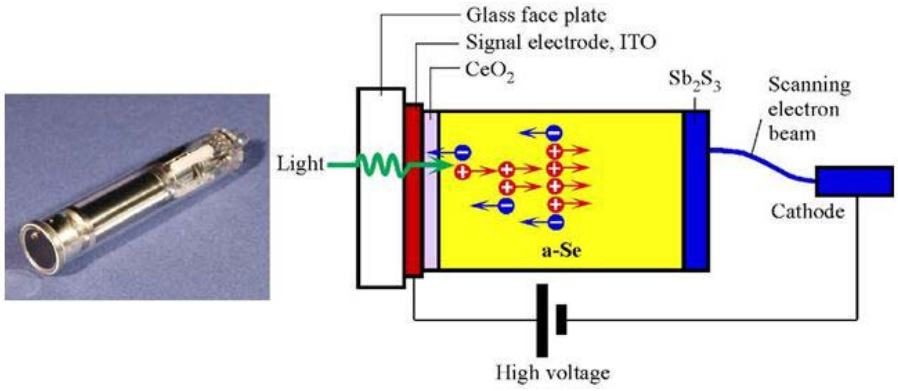

Figure 2.3: Left: A HARP tube is a TV pick-up (video) tube with avalanche gain; it is called a Harpicon. Right: A schematic illustration of the HARP and its operation under avalanche. (Courtesy of Dr. Kenkichi Tanioka, NHK, Japan.)

Figure 2.4. A snap-shot image from a real time movie of a rainbow formed under moonlight at night at Iguazu Falls, Brazil, taken by a HDTV-Harpicon. (Courtesy of Dr. Kenkichi Tanioka, NHK, Japan.)

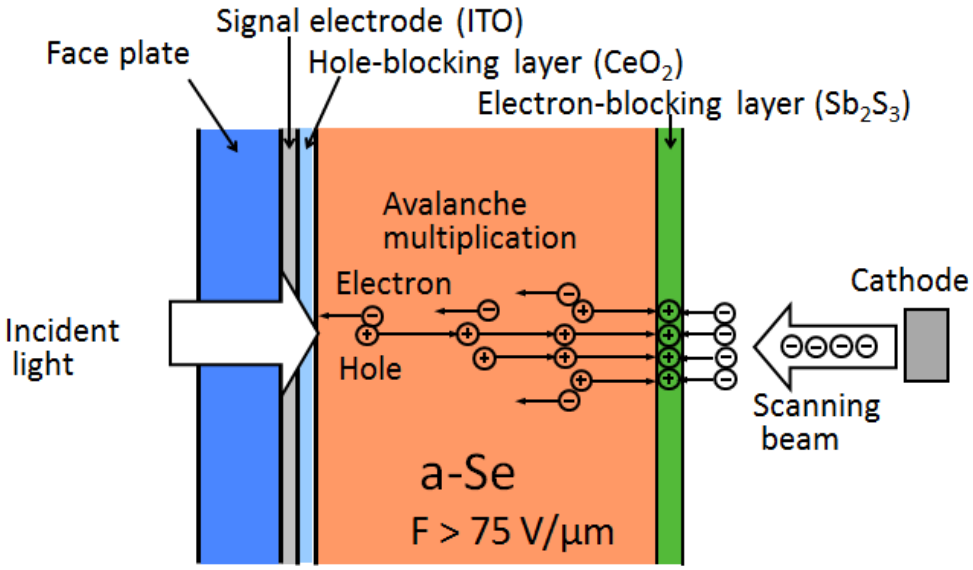

Figure 2.5: Avalanche a-Se HARP structure with electron beam read out operating in avalanche regime.

For electric fields below the avalanche multiplication threshold (F < 75 V/µm), holes drift across the a-Se layer at a constant drift velocity given by the product of their mobility and electric field. The charge collected by the electrodes is equal to the number of EHPs created by the photons, resulting in a gain of unity. Above the avalanche multiplication threshold (F > 75 V/µm), the holes gain enough kinetic energy between collisions to create additional EHPs along their paths by impact ionization. This increase in EHPs in the a-Se layer is called avalanche multiplication, and the resulting internal gain is called the avalanche gain. It is also possible for electrons to initiate impact ionization and contribute to avalanche gain, but it has been shown that this effect is negligible for F < 105 V/µm. When both charge carriers undergo avalanche, dark current increases exponentially and the device is on the verge of breakdown. Therefore, our analysis is limited to F < 105 V/µm where electron avalanche can be ignored.

2.3.2. a-Se with metal electrodes

Practical a-Se HARP photosensors had previously been restricted to signal readout using a scanning electron beam, which requires a vacuum operation [42,43,44]. For use in

medical imaging systems, the electron beam has to be replaced by a two-dimensional array of pixel electrodes [39]. However, implementation of electronic readout to HARP structure has several technological challenges.

There have been some efforts to develop a solid-state HARP photodetector, in which the metal electrode is deposited on the HARP layer. Two Japanese groups have demonstrated avalanche multiplication in in this case, but with limited success [51,52]. Ohshima et al. obtained an avalanche gain of up to 10 times in a-Se layers 1-6 μm thick coated with a gold electrode [51]. A similar gain was obtained by Takiguchi *et al*. in 500 nm thick a-Se coupled to a complementary metal oxide semiconductor (CMOS) readout layer [52]. But in these devices, stable operation without breakdown was not possible. Firstly, metal contacts may degrade. Previous attempts to fabricate pixelated electrodes using gold (Au) have been unsuccessful, with higher noise observed compared to the electron beam readout [51]. This excess noise can be attributed to the gradual diffusion of Au into a-Se. Secondly, sporadic dielectric breakdown at the edges of metal electrodes may occur. This can happen because the high electric fields required for avalanche is further increased at the contact edge (Figure 2.6). An incipient breakdown causes a high current flow that can induce a phase transition due to Joule heating. This may result in irreversible crystallization of an area adjacent to contact [53]. The permanent structural defect at the edge of the contact due to breakdown is shown in Figure 2.7.

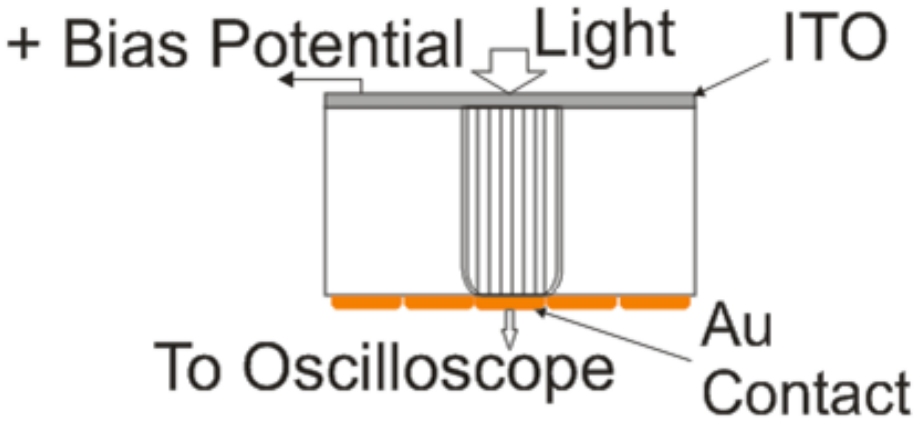

Figure 2.6: Schematic of increased electric field at the contact edge in avalanche a-Se HARP structure with pixel electrodes operating in avalanche regime.

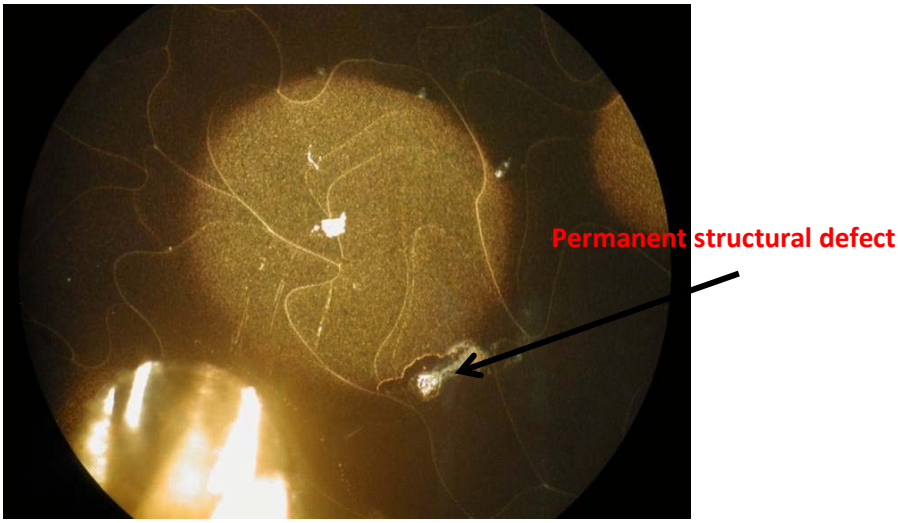

Figure 2.7: Picture of avalanche a-Se HARP structure with Au electrode where permanent structural defect occurred due to dielectric breakdown.

The measured dark current characteristic before and after breakdown is shown in Figure 2.8.

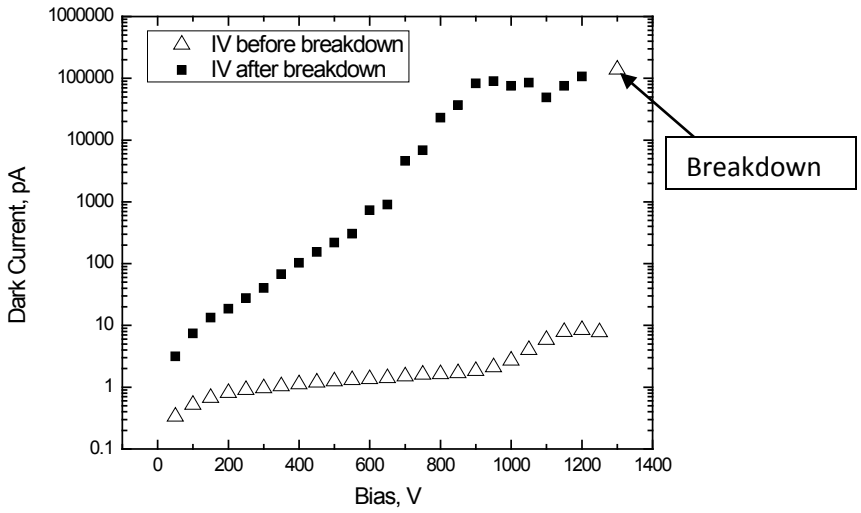

Figure 2.8: The variation of Dark Current to applied bias of avalanche a-Se HARP structure with Au electrode before and after breakdown.

2.3.3. a-Se with Resistive Interface Layer (RIL) and metal electrodes

The above challenges have hindered the development of electronic readout methods for avalanche a-Se photoconductors. Enabling stable operation of pixelated a-Se avalanche

photosensors without contact degradation, sudden breakdown and associated structural transformations is an important issue in avalanche a-Se technology. We have shown previously that incipient breakdown can be prevented by coating the HARP free surface with a Resistive Interface Layer (RIL) made of a semi-insulating polymer, namely cellulose acetate (CA) [54]. CA has been chosen as the RIL for the modified a-Se HARP structure as it bonds well to a-Se and is compatible with a-Se technology: CA has been used as a protective coating in a-Se xeroradiographic plates and in this application extended the plate life by a factor of approximately 10 [55]. Although an improvement of stability against breakdown was evident with our results [54], concern remained regarding possible degradation of transport properties. This issue is addressed here. By analysis of transport properties, we show that while improving HARP blocking characteristics, a thin (~ 1μm) RIL does not degrade its transport properties: no charge trapping at HARP/RIL interface layer was observed and no deterioration of transient response was found. Furthermore, a RIL prevents gold diffusion into a-Se structure. The above features make RILs a practical approach for the development of a-Se solid-state avalanche photosensors with extremely low dark current for a variety of applications in optical imaging and PET.

The deposition of a RIL is done in a clean room under well controlled parameters. These parameters are acceleration, deceleration, speed, temperature and amount of CA to deposit. The schematic presentation of deposition process is shown on figure 2.9. The crucial part of depositing a RIL is the environment in which you perform a deposition. In order to control this, the entire deposition process was done under a nitrogen flow and a well-controlled temperature.

To model the effect of CA on the electric field distribution, the PSpice program was used. This program allows us to see the effect of a RIL on a-Se from an electrical circuit point of view. At a fixed bias, we model the detector as an ideal current source in parallel with a capacitor and a resistor. The resistor accounts for the dark current in the detector and, since the dark current is non-linearly dependent on bias, the resistor is also bias dependent. This model is shown in Figure 2.10.

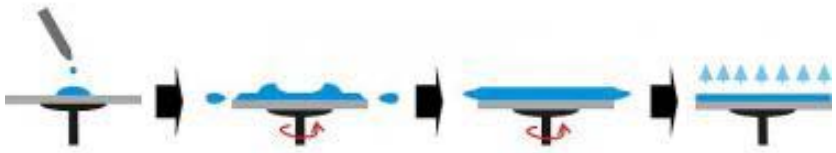

Figure 2.9: Diagram illustrating the cellulose acetate (CA) casting process. A controlled amount of CA solution is first dispensed on the HARP target which is securely mounted on a spin-coater plate by vacuum. Then the sample is covered with CA. Next, the solvent in the CA solution is given time to evaporate. To make thin and uniform layer during the evaporation process the plate is rotating. The HARP target is then removed from the plate.

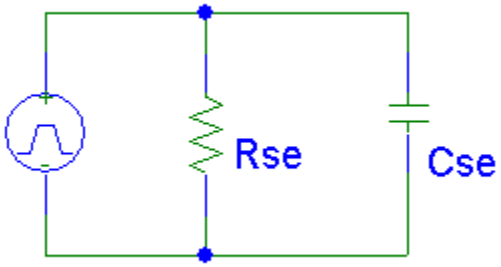

Figure 2.10: Schematic representation of a-Se and RIL from electrical point of view.

The photodetector capacitance depends on its thickness, dielectric constant and contact area. Assuming parallel plate geometry and neglecting fringing field:

$$C_{Se} = \varepsilon_{Se}\varepsilon_0 \frac{A}{d}\ , \tag{2.1}$$

where: A is the contact area, d is the detector thickness, ε_0 is permittivity of vacuum, ε_{Se} is the relative dielectric constant of the photodetector.

The value of R_{Se} is calculated ad-hoc from the applied bias and the measured dark current at that bias.

The polymer is modeled simply as a resistor in parallel with a capacitor as shown in figure 2.11

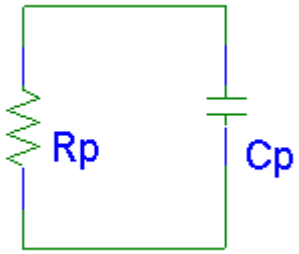

Figure 2.11: Electrical model of the RIL.

The polymer capacitance is also calculated according to Equation 2.1. The resistance is inferred from separate measurements on electroded polymer layers. The detector-polymer structure is therefore electrically modeled as in figure 2.12 The 50 ohm resistor represents the input of an oscilloscope or another low impedance measuring system.

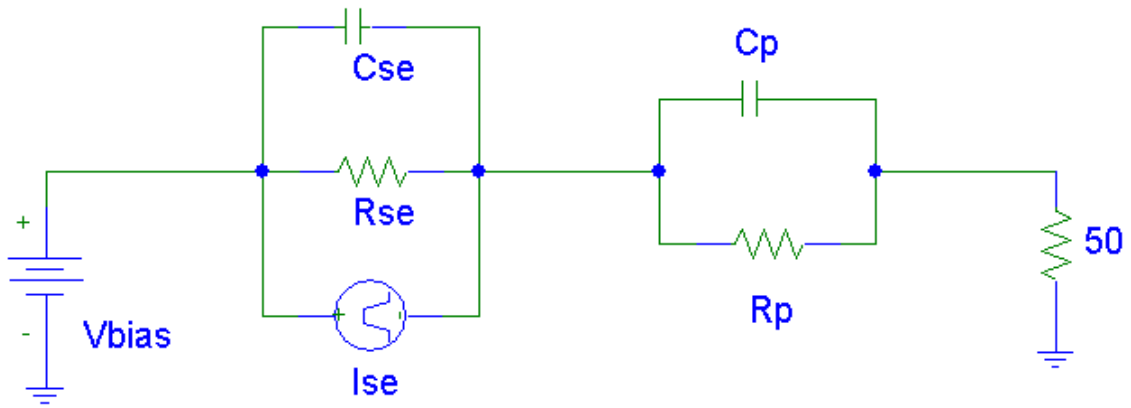

Figure 2.12: Electrical model of the a-Se with RIL connected to the high voltage power supply and 50 Ohm Oscilloscope input.

In DC mode in the absence of illumination, the capacitances may be ignored and the detector signal current I_{Se} is zero. Since the polymer resistance is in series with the detector the actual detector bias is reduced by an amount ΔV :

$$\Delta V = I_{dark} R_P \tag{2.2}$$

This drop is normally negligible. For a 100 pA dark current and a polymer resistance of 10 Gohm it amounts to 1 Volt. The drop on the 50 ohm scope resistance is much smaller and may be safely ignored.

In AC mode, when a pulse of light is applied to the detector it responds with a current pulse (I_{Se} is non-zero). In this mode, given the shortness of the signal pulses in comparison with the *RC* time constants of the detector and polymer, we can ignore the detector and polymer resistances and consider only their capacitances. Also the bias may be considered as a ground potential. The equivalent circuit in this mode may be conveniently redrawn as shown below.

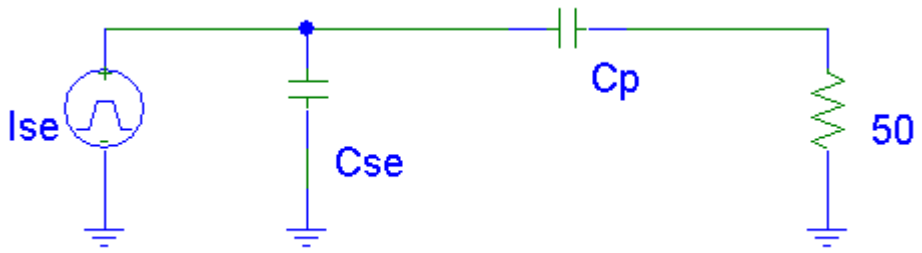

Figure 2.13: Electrical model in AC mode of the a-Se with RIL connected to the high voltage power supply and 50 Ohm Oscilloscope input

As we can see from this circuit, the effect of the polymer is a reduction in the collected signal charge. Only the charge flowing through the polymer capacitance will be collected by the oscilloscope. The remaining charge is left on the detector capacitance. The efficiency of charge collection is given by the ratio:

$$\eta = \frac{C_P}{C_P + C_{Se}} \tag{2.3}$$

In practice, given that the thickness of the polymer is much less than that of the detector and, consequently, the capacitance of the polymer is much higher, this ratio is close to

unity. It must be noted that the uncollected signal eventually dissipates into the circuit resistances.

2.4. Methods

2.4.1. Optical time-of-flight

The Time-Of-Flight (TOF) technique [56] was used to investigate transport and charge collection in both types of a-Se photosensors. TOF transient photoconductivity measurements serve as a very useful tool in studying the transport and multiplication of charge carriers in the modified-HARP device. This methodology was used because of a few reasons. Firstly, a-Se is a high impedance material, its resistivity can vary from 10^9 *Ohm•cm* to 10^{16} *Ohm•cm* depending on production technique. A large resistivity results in a long Maxwell relaxation time τ_m. This allows us to do experiments where the time of travel of carriers (t_{tr}) is less than the Maxwell relaxation time ($t_{tr} << \tau_m$). Secondly due to the short absorption depth in a-Se at 420 nm, electron-hole pairs (EHP) are generated close to the ITO/a-Se interface. The photogenerated holes traverse a distance equal to *d*, whereas the photogenerated electrons travel only a very short distance to the ITO contact. The duration of the laser pulse is negligible in comparison with both the *RC* constant of the a-Se layer and the transit time for holes under all experimental conditions. All measurements were made at room temperature. Current transients for holes allowed us to calculate hole transient time and mobility. Meanwhile, the integration of transient photocurrents allowed us to obtain the kinetics of charge collection at different electric field regimes. This in turn permits us to derive the ratio between total collected electrons and holes (n_e / n_h). The importance of this ratio is that it allows an accurate calculation of the avalanche gain at different fields.

2.4.1.1. Experimental apparatus

For TOF measurements, photosensors were exposed from the ITO side to a short (35 ps) laser pulses with wavelength of 420 nm (which corresponds to the peak emission from scintillation crystals used in PET) and the current transients were monitored at various applied electric fields, F, by a 6 GHz bandwidth digital oscilloscope (Figure 2.14). In

both types of a-Se photosensors, the electric field across the a-Se layer was created by connecting a positive voltage supply to an ITO layer (Figure 2.14). The range of applied electric fields was 10-104 V/µm for Type 2 samples (with RIL) and 10-80 V/µm for Type 1 (w/out RIL). Fields applied to Type 1 samples were restricted to prevent the dielectric breakdown which was found to occur above 80 V/µm after a few seconds of operation. It should be noted that in a signal mode (i.e. when a photosensor is exposed to a very short light pulse) the presence of CA layer does not affect the photocurrent.

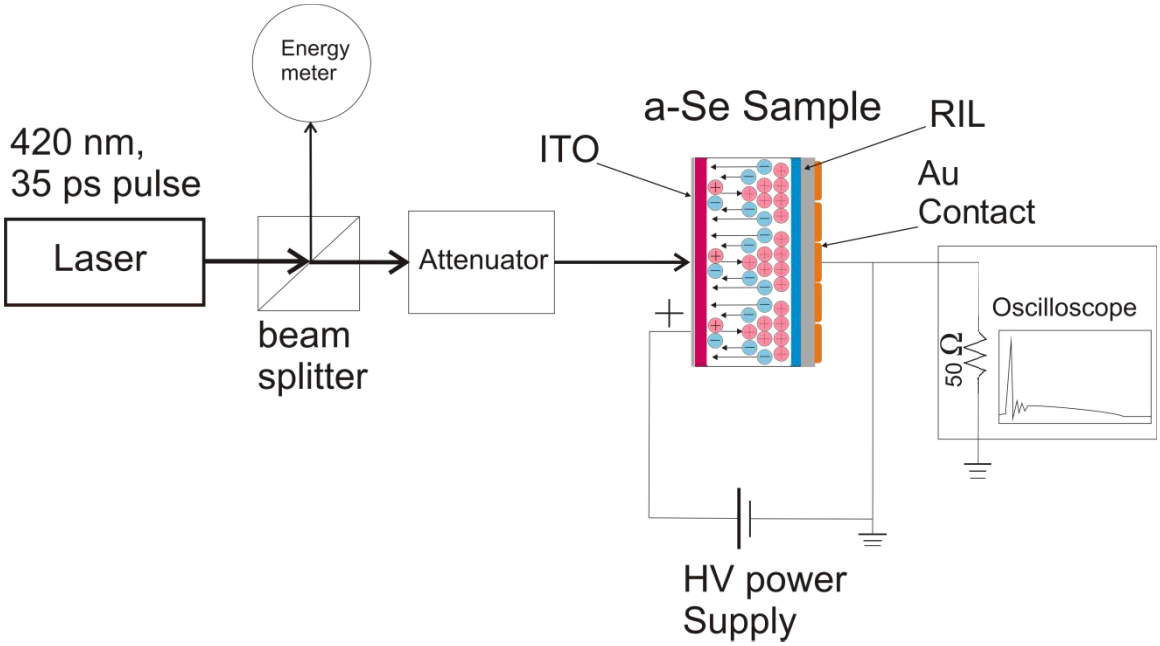

Figure 2.14: Schematic representation of Time-Of-Flight experimental apparatus which is used for measurement of electron-hole pair generation in a-Se.

2.4.2. Dark Current kinetics measurement

The dark current of the photoconductor under a bias voltage should be negligibly small. The dark current in most photoconductive semiconductors is normally attributed to one of two factors—the rate of injection of carriers from the contacts into the photoconductor and the rate of thermal generation of carriers. A small dark current implies that the contacts to the photoconductor should be non-injecting, and the rate of thermal generation of carriers from various defects or states in the bandgap should be negligibly small (*i.e.*, dark conductivity is practically zero). Small dark conductivity generally

requires a wide bandgap semiconductor that conflicts with the condition of smaller ionization energy. There have been several attempts to estimate what would constitute a negligible dark current density, J_d [17]; it is generally accepted that J_d should preferably not exceed 10 pA mm^{-2} depending on the clinical application.

2.4.2.1. Experimental apparatus

Dark current decay was measured as a function of time for different bias voltages on all types of photosensors. During this measurement, the sample was kept in complete darkness to prevent the generation of photocurrent. The sample was biased using a programmable high voltage power supply (Stanford Research PS350) and a programmable electrometer (Keithley 35617EBS) was used to measure the dark current. The measurements were performed under computer control and, for each bias, dark current data was acquired at 1s intervals for 10000 seconds. The sample was allowed a 12 hour resting period in complete darkness and zero bias, before proceeding to a new bias. During this resting period, the dark current data was also acquired at 1s intervals, we call this measurement *recovery*.

2.5. Results

2.5.1. Optical time-of-flight

Our results confirm that modified HARP structures with 1 μm thick CA layer as RILs can withstand a very high electric field (about 100 V/μm) without electrical breakdown: Also, high electric fields could be cycled up and down many times with no change in properties. In contrast, standard HARP photosensors without CA coating and with metal electrodes undergoe breakdown after few seconds of operation if biased at about 80 V/μm or higher (Figure 2.8). However, the presence of a foreign layer like a RIL may in principle enhance charge trapping at the a-Se/RIL interface, deteriorating transient performance. TOF measurements were performed to clarify this issue. Figure 2.15 shows photocurrent pulses at electric fields below avalanche multiplication and Figure 2.16 shows photocurrent above avalanche multiplication threshold F_{AV}.

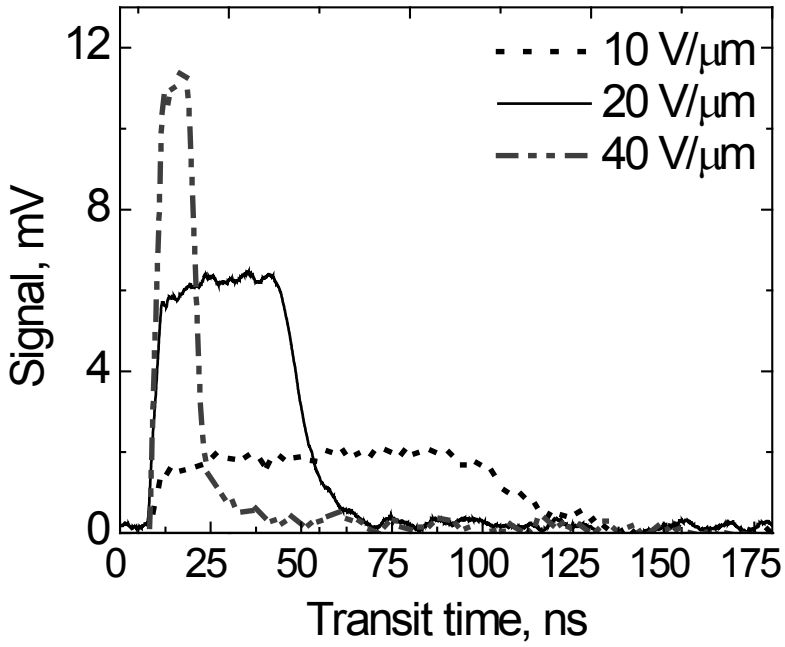

Figure 2.15: Hole transit time curves for modified a-Se HARP blocking structure (with RIL (Type 2)) at different field intensities in the non-avalanche region.

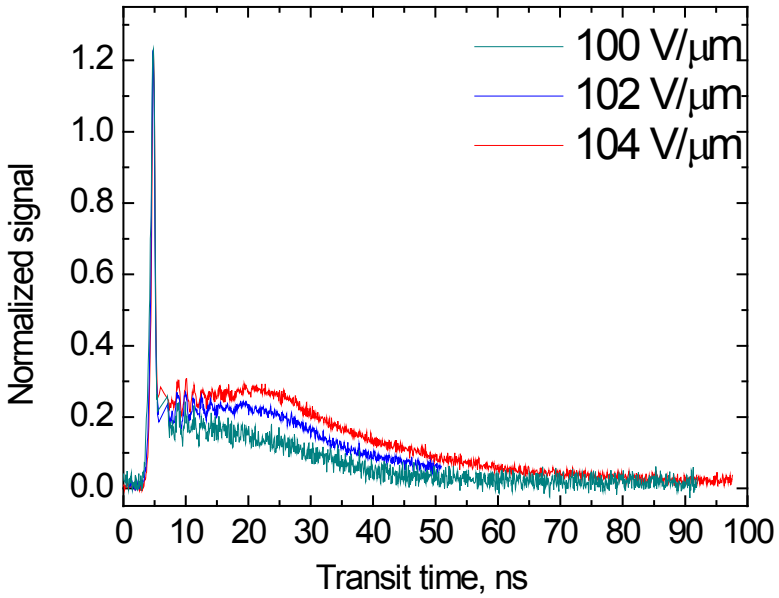

Figure 2.16: TOF signal from a-Se HARP blocking structure with RIL (Type 2) in avalanche regime for electric field 100 V/μm, 102 V/μm and 104 V/μm.

As it is seen from Figure 2.15, the hole transient profile for Type 2 structures at $F < F_{AV}$ has a quasi-rectangular shape with a well-defined knee, which corresponds to the hole transit time t_h (photogenerated electrons do not contribute significantly to the photocurrent since they are captured rapidly upon photogeneration, traveling a very small distance to the positive electrode). The Figure 2.17 compares hole transients for Type 1 and 2 samples at the same bias of 300 *V*. The similarity in photocurrent indicates that both transport properties and t_h are unaffected by the presence of RIL.

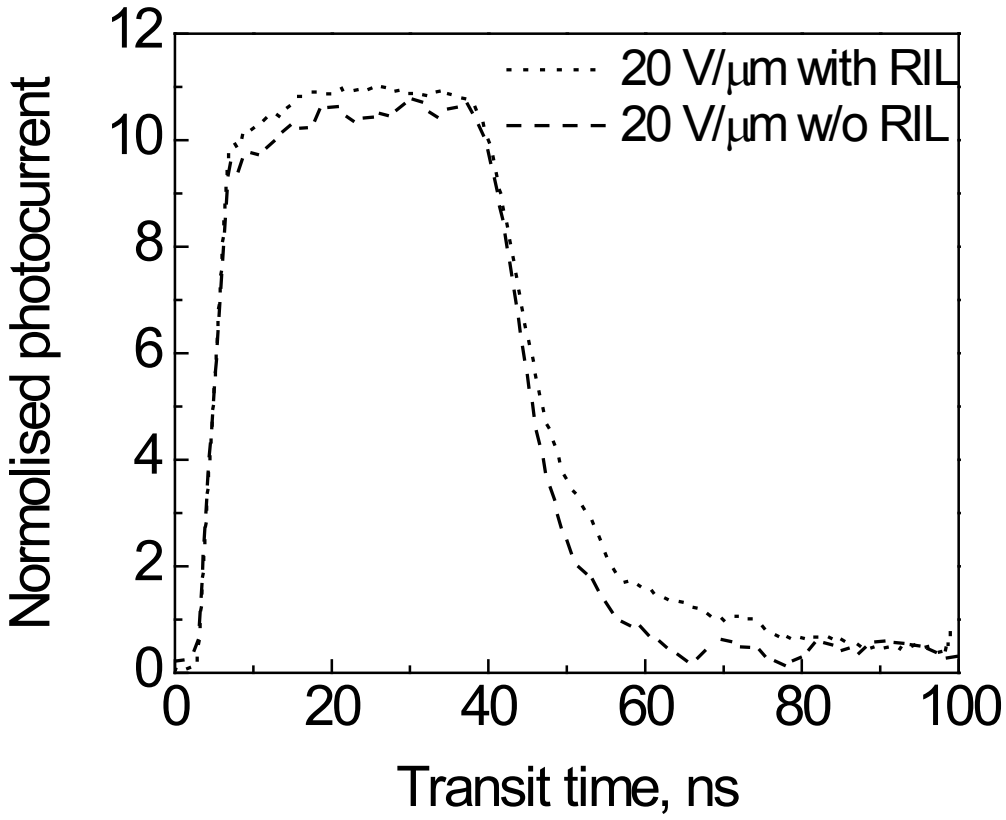

Figure 2.17: Shows hole transit time curves comparison between a-Se HARP blocking structure with and without RIL in the non-avalanche region.

The shape of the photocurrent in an avalanche regime $(F > F_{AV})$ is different from that of a non-avalanche regime (Figure 2.18) and exhibits a rapid increase due to the motion of avalanching holes followed by a comparatively long tail due to the slow motion of secondary non-avalanching electrons which are created in the trail of avalanching holes.

An integrated TOF curve on Figure 2.19 shows the charge collection curve at a selected field *F=100 V/μm* (above the avalanche multiplication threshold). As it is evident from Figure 2.19, the fast leading edge due to the collection of avalanching holes is followed by a comparatively slow rise due to the collection of much slower non-avalanching electrons.

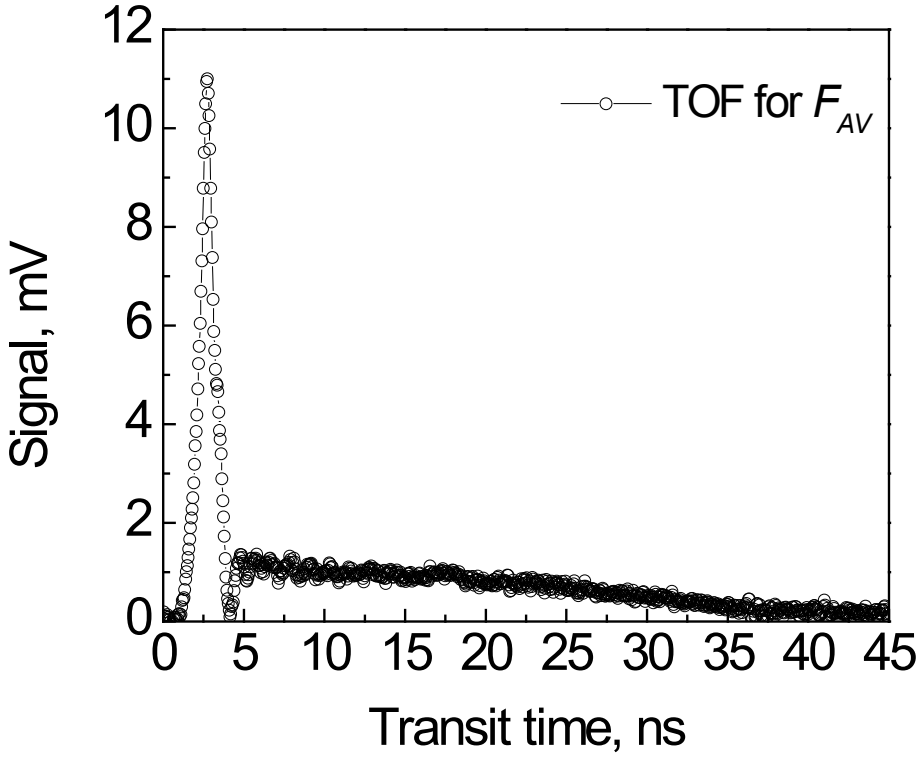

Figure 2.18: TOF signal from a-Se HARP blocking structure with RIL (Type 2) in avalanche regime for electric field 100 V/μm.

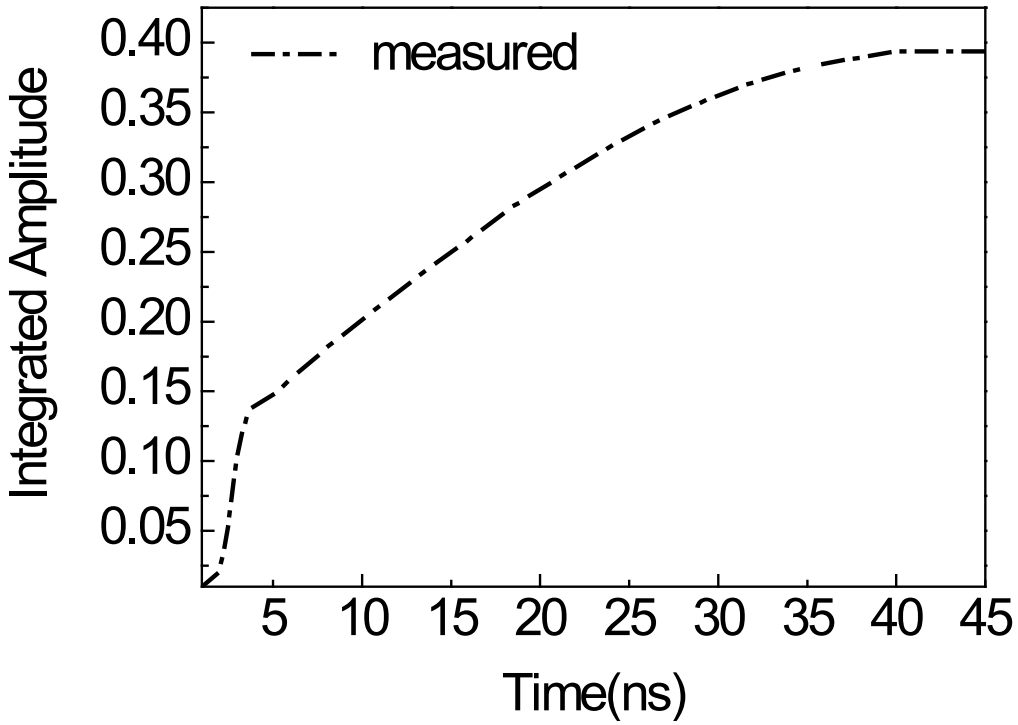

Figure 2.19: Variation with time, of the integrated TOF signal at 100 V/μm from a-Se HARP blocking structure with RIL (Type 2) in avalanche regime.

2.5.2. Dark Current Decay

The mechanism of dark current decay (Figure 2.20) is not clearly understood and should be investigated further. However, for all types of samples, the dark current decays by approximately 2 orders of magnitude and saturates at low values. For example, for Type 3 structures, the steady state dark current was about 2 pA/mm2 at a comparably high electric field of 60 V/μm. More detailes about the nature of Dark Current Kinetics in a-Se is in Section 2.6.2

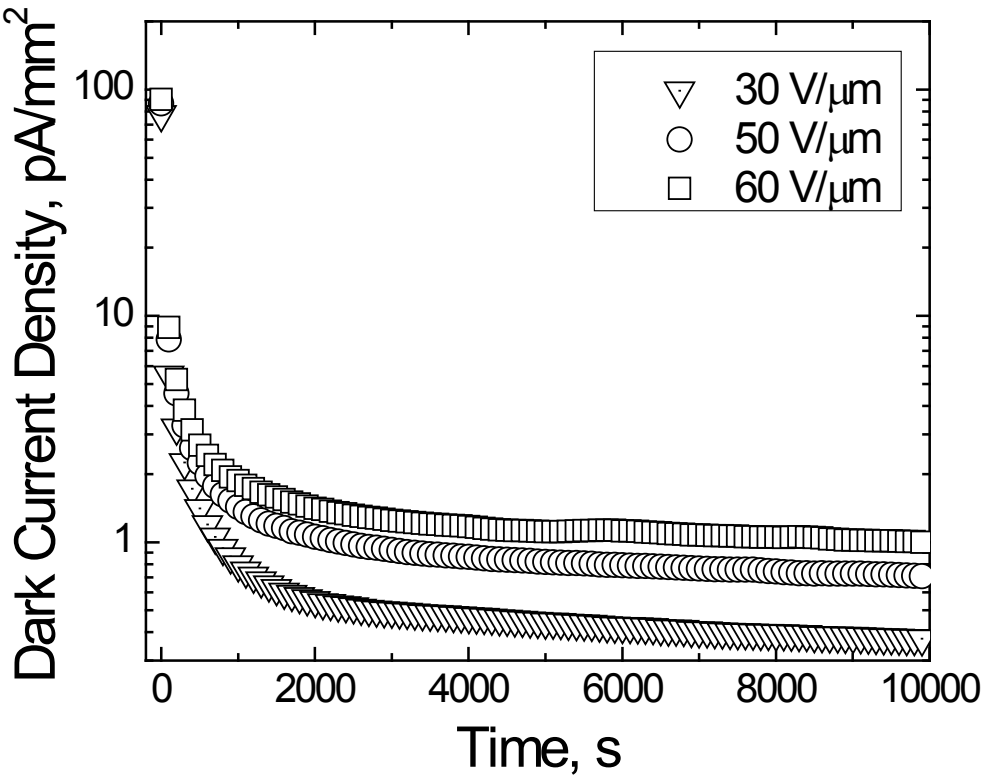

Figure 2.20: The dark current decay for a-Se incomplete HARP blocking structure with RIL (Type 3) sample. The dark current decays with time almost in two orders of magnitude.

2.6. Discussion

2.6.1. Optical time-of-flight

2.6.1.1. Transient current

Comparative analysis of charge transport in standard and modified HARP structures clearly show that there is no noticeable trapping at the a-Se/CA boundary. At sub-avalanche regimes, transport in Type 2 structures remains non-dispersive like in "virgin" (Type 1) HARP structures and in a-Se insulating structures [57]: in both Type 1 and Type 2 structures a constant current and well-defined transit time (Figure 2.17) have been observed. Furthermore, as it is seen in Figure 2.21, hole mobilities in non-avalanche

regimes are identical for Type 1 and Type 2 structures. The field dependence of hole drift mobilities for $F<F_{AV}$ is similar to that observed for a-Se insulating structures: mobility increases rapidly with the field and reaches the value ~ 0.8 cm^2/Vs at the threshold of avalanche multiplication F_{AV} [57]. Because of breakdown, it was impossible to measure hole mobility in avalanche regime ($F>F_{AV}$) for Type I samples. These measurements were done for Type II samples with a RIL only.

2.6.1.2. Charge carrier mobility

The slope change in integrated curves allows us to define the hole transit time t_h while saturation of the total collected charge allows us to define electron transit time t_e in avalanche regime. From the measurements of t_h and t_e we derive drift mobilities for holes and electrons, t_h and t_e, respectively:

$$\mu_h = \frac{d}{t_h F}, \qquad \mu_e = \frac{d}{t_e F}, \tag{2.4}$$

Field dependence of hole drift mobility, μ_h, is shown in Figure 2.21. As it can be seen from Figure 2.21, hole mobilities at $F<F_{AV}$ are similar for both types of photosensors. Electron drift mobility, μ_e, was found to be almost field independent in the range of F under consideration and with a magnitude of 0.06 $cm^2/(Vs)$ (Figure 2.22). Electron and hole mobilities derived from the analysis of our TOF measurements were compared with the corresponding findings for a-Se insulating structures which have been used by Juska and Arlauskas [57,58] to demonstrate avalanche multiplication phenomenon in a-Se. In this work, the a-Se monolayer was confined between two insulating layers permitting application of the high electric field needed for avalanche without charge injection. Schematic representation of this structure is shown on Figure 2.23. Although insulating structures cannot be used as practical photosensors (as no exit of mobile charge is possible because of insulating layers) they serve as a baseline for our research.

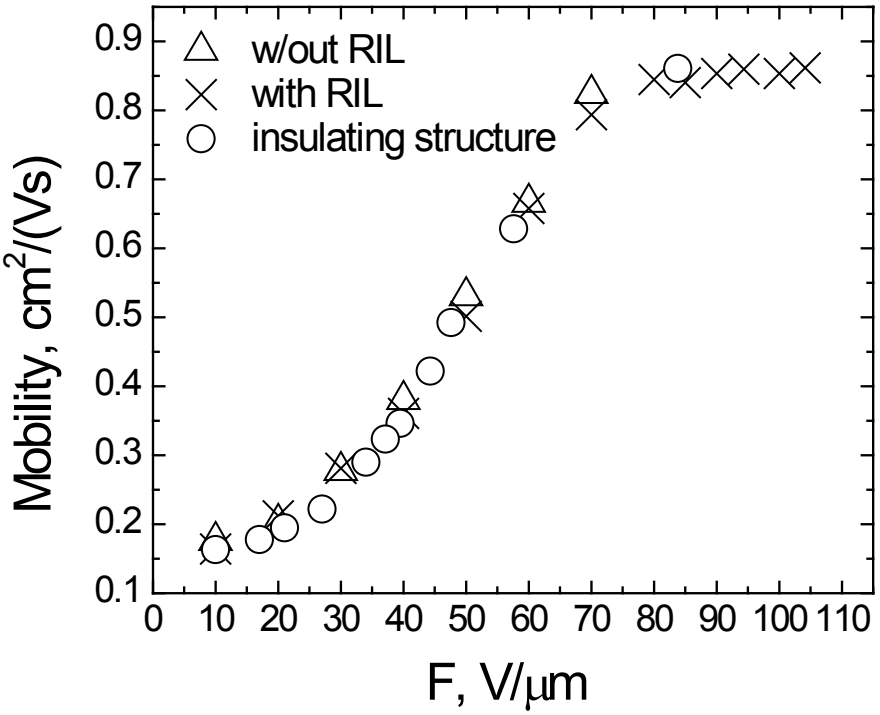

Figure 2.21: The Comparison of hole-mobility for a-Se HARP blocking structure with RIL (Type 2), a-Se HARP blocking structure (Type 1) and a-Se insulating structure. As it is seen from plot the mobility is almost identical and not affected by the presence of an extra layer.

As it is seen in Figure 2.21, at $F \geq F_{AV}$, holes propagate with mobility which nearly does not depend on the field. This is a "prototype" behaviour for hole mobility in a-Se where hole transport is controlled by trapping into localized states within the band tails. An increase in electric field results in the heating of holes and the transition to field independent microscopic mobility at the threshold of avalanche multiplication [58]. This transition agrees well with the modified Lucky Drift (LD) model recently suggested for the explanation of avalanche multiplication in amorphous solids [59]. Indeed, the modified LD model requires carrier to move without trapping as a prerequisite for impact ionization. The microscopic mobility, μ_0, for a-Se insulating structures was found to be 0.8 cm^2/Vs [58] which is in excellent agreement with our results.

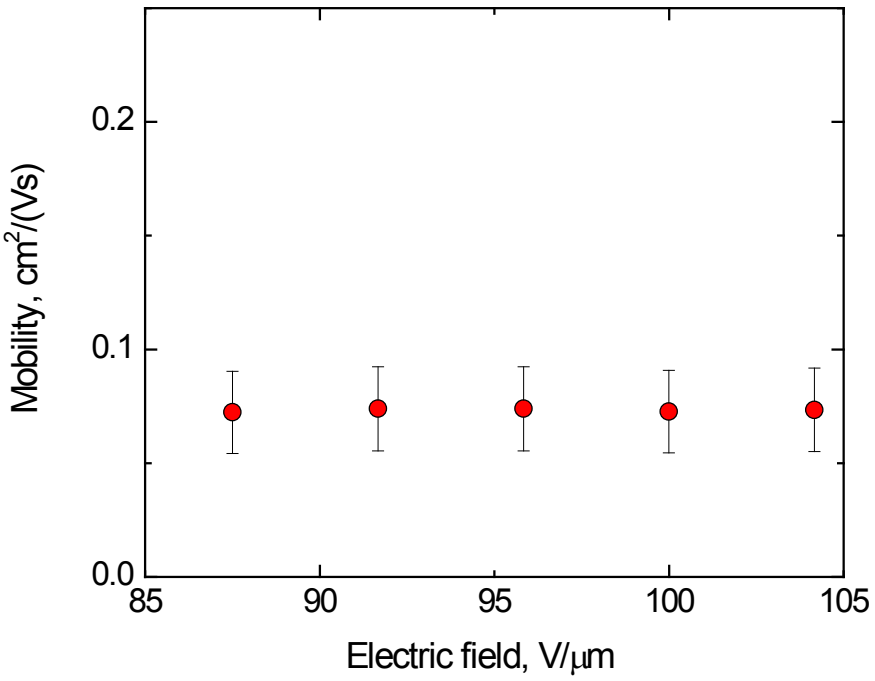

Figure 2.22: Electron drift mobility at high electric field from a-Se HARP blocking structure with RIL (Type 2) in avalanche regime.

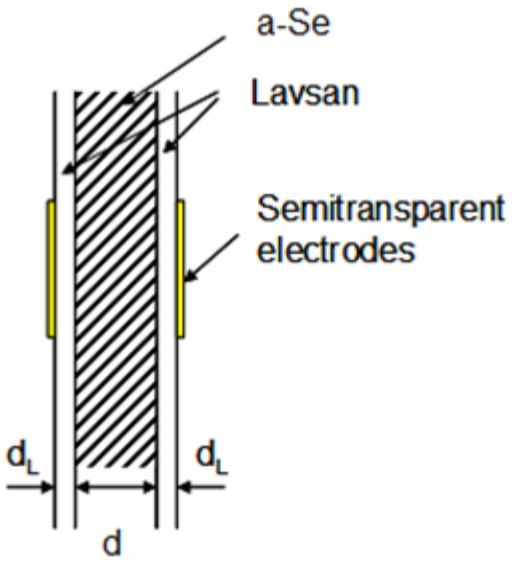

Figure 2.23: Schematic representation of insulating structure. Were a-Se is confined between two completely insulating layers.

Electron drift mobilities were calculated for Type 2 structures for $F>F_{AV}$ Figure 2.22 and were found to be field independent with a magnitude of 0.06 $cm^2/(Vs)$ which is also in good agreement with the results obtained for a-Se insulating structures [58].

2.6.1.3. Photoresponse model

Thus obtained mobilities have been used as input parameters for the simulation of theoretical photoresponse in avalanche regime. For this simulation an analytical expression for the avalanche current was derived based on the following assumptions:

a) only holes can avalanche at applied fields; electrons do not avalanche with mobilities more than an order of magnitude smaller than those for holes (0.06 cm^2/Vs for electrons vs 0.8 cm^2/Vs for holes);

b) avalanche occurs uniformly through the a-Se thickness with multiplication coefficient which depends exponentially on traversed distance *x* [40];

c) the photocurrent is not space-charge perturbed (the amount of charge in the bulk does not significantly affect the field). Under these assumptions and using Ramo's theorem, the induced current due to drift of avalanching holes is:

With these assumptions the number of holes (initial plus those due to avalanche) generated per unit volume in the detector when the charge sheet reaches position x is given by:

$$n_h(x) = n_0 e^{\gamma_p x} \tag{2.5}$$

Parameter γ_p accounts for avalanche gain and is field dependent; n_0 is the initial hole concentration (generated at *x=0*). Eq. 2.5 can be derived by considering the increment in the hole concentration $dn_h = \gamma_p n_h(x)dx$ when the position is incremented from *x* to *x+dx*, and integrating.

Since electrons and holes are generated in pairs, the same equation applies for electrons:

$$n_e(x) = n_0 e^{\gamma_p x} \tag{2.6}$$

Within the transit time of holes, the holes current is proportional to n_h and the velocity of holes. The velocity of holes may be written as:

$$v_h = \mu_h F \tag{2.7}$$

where μ_h is the hole drift mobility and F is the applied electric field. Note that the drift mobility is field dependent. We perform a change of variable from space to time using:

$$x = v_h t = \mu_h F t \tag{2.8}$$

Then we obtain the hole current density:

$$\begin{cases} I_h(t) = ep_0 \dfrac{\mu_h F}{d} \exp(\gamma_p \mu_h F t), t < t_h \\ I_h = 0, t > t_h \end{cases}, \tag{2.9}$$

where e is the elementary electron charge, $t_h = \dfrac{d}{\mu_h F}$ is the hole transit time and d is the detector thickness. Here we made use of the fact that current density is the product of charge density and velocity.

To calculate the electron current density we must take into consideration the fact that, although the electron mobility is much smaller than the hole mobility, the electrons are initially generated close to the positive electrode and move towards it. As the holes propagate and avalanche, some of the electrons will travel to and recombine at the positive electrode. Therefore, in order to calculating the electron current at a given time we must subtract those electrons. When the holes have reached position x the total number of electrons generated is $n_e(x)$ and the number of electrons that have crossed the

positive electrode boundary is $n_e\left(\frac{\mu_e}{\mu_h}x\right)$. The net number of electrons left in the detector when the holes reach position x is therefore:

$$\Delta n(x) = n_e(x) - n_e\left(\frac{\mu_e}{\mu_h}x\right) \tag{2.10}$$

or

$$\Delta n(x) = n_0 \exp(\gamma_p x) - n_0 \exp\left(\gamma_p \frac{\mu_e}{\mu_h}x\right) \tag{2.11}$$

From this equation we can derive the electron current similarly to what we did for holes.

As we did for holes we define the electrons transit time as $t_e = \frac{d}{\mu_e E}$. Because the electrons propagate slower than holes we have to consider three time intervals:

$t < t_h$, when electron-hole pairs are being generated;

$t_h \le t < t_e$, holes have moved out, no further avalanche occurs but some electrons are still drifting in the detector;

$t \ge t_e$, all electrons and holes have moved out of the detector.

With this in mind we first make the change of variables:

$$\begin{cases} \Delta n(t) = n_0 \exp(\gamma_p \mu_h F t) - n_0 \exp\left(\gamma_p \mu_e F t\right), t < t_h \\ \Delta n(t) = n_0 \exp(\gamma_p d) - n_0 \exp\left(\gamma_p \mu_e F t\right), t_h \le t < t_e \end{cases} \tag{2.12}$$

The induced current due to the drift of non-avalanching secondary electrons is:

$$\begin{cases} I_e(t) = e n_0 \frac{\mu_e F}{d}[\exp(\gamma_p \mu_h F t) - \exp(\gamma_p \mu_e F t)], t < t_h \\ I_e(t) = e n_0 \frac{\mu_e F}{d}[\exp(\gamma_p d) - \exp(\gamma_p \mu_e F t)], t_h \le t < t_e \\ I_e = 0, t \ge t_e \end{cases} \tag{2.13}$$

where $t_e = \frac{d}{\mu_e F}$ is the electron transit time, γ_p is the hole impact ionization coefficient, n_0, p_0 is the number of electrons and holes, respectively, injected by a pulse of light at the positive contact.

The total avalanche current is the sum of hole and electron currents:

$$I_A = I_h + I_e \tag{2.14}$$

Equation 2.14 has been used to simulate the total photocurrent at avalanche regime using experimentally measured field dependencies μ_h, μ_e and γ_p [40]. Experimental and theoretical results agree well as it is seen from Figure 2.24, showing the validity of our analytical approach.

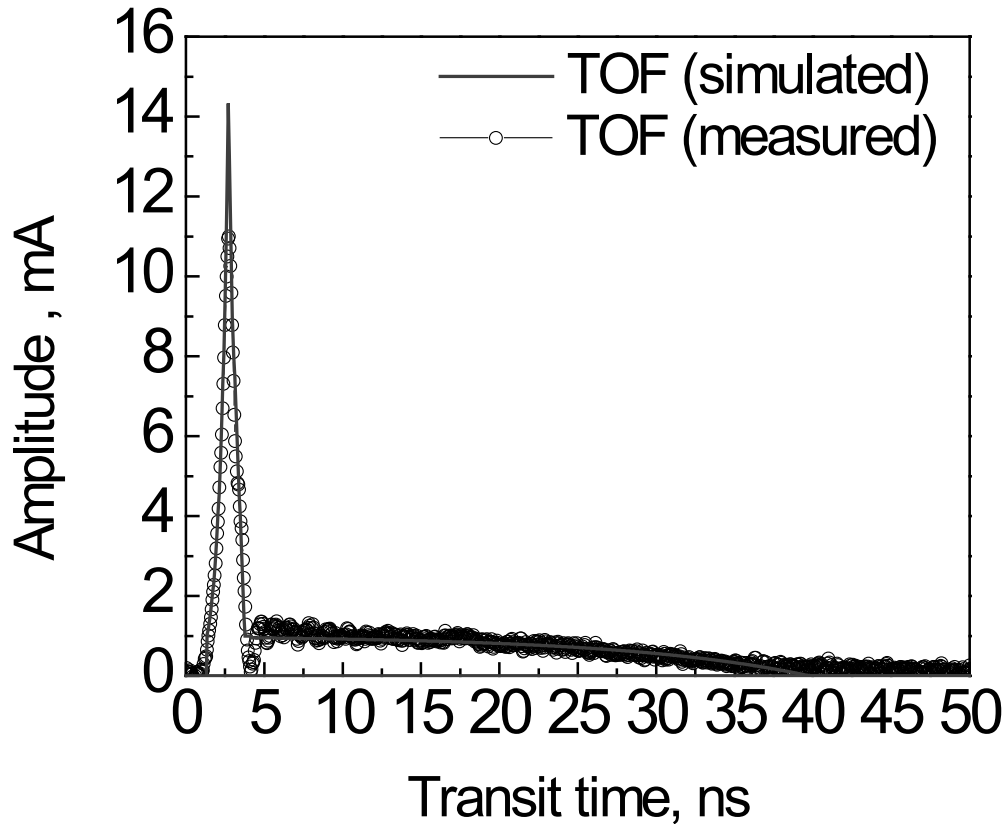

Figure 2.24: Comparison of TOF signal from a-Se HARP blocking structure with RIL (Type 2) in avalanche regime for electric field 100 V/μm with simulated curve using

experimental parameters. The measured photocurrent corresponds very well to simulated results.

2.6.1.4. Avalanche gain

Charge collection curves (Figure 2.25) have been used to analyze the relative contribution to photocurrent of secondary electrons and holes created as a result of impact ionization. Figure 2.25 shows the integrated photocurrent and the integral curve obtained by simulation in section 2.6.1.3. The field dependence of electron-to-hole ratio (n_e/n_h) calculated from the charge collection curves are shown in Figure 2.26. As it is seen from Figure 2.26, at comparatively low fields (below ~ 95 V/μm) $n_e/n_h<1$. This means that holes contribute more to the externally measured charge than electrons. At higher fields, n_e/n_h exceeds unity and electrons become the major contributors to the measured signal. The inequality occurs because the charge induced in the external circuit depends on the distance traveled by a carrier as a fraction of detector thickness (Figure 2.27). This distance in turn depends on the depth within the detector at which the impact ionization occurs and the charge is generated. At $g_{AV}=1$ electrons are created very close to the positive electrode and are rapidly collected with negligible contribution to the measured TOF signal, while the holes travel nearly the entire depth of the detector, towards the negative electrode, creating the TOF signal. Therefore for $F \leq F_{AV}$ the contribution to the signal is almost entirely due to holes. On the other hand, at $F>F_{AV}$, as the drifting holes cause impact ionization, electrons are created at larger distances from the positive electrode and they start to contribute to the TOF signal while traveling towards the positive electrode. At a gain of 5.2, the electrons and holes equally contribute to the TOF signal. The multiplication coefficient g_{AV} depends exponentially on the distance traveled, according to this equation:

$$g_{AV}=exp(\gamma_p d) \tag{2.15}$$

The higher the gain, the more secondary electron hole pairs are created close to the negative surface of a-Se. Consequently, holes are rapidly collected at the negative pole with minor contribution to the TOF signal. Meanwhile, electrons traverse the entire thickness of the layer back to the positive electrode, thus contributing significantly to the

measured signal (Figure 2.27). At 104 V/μm, the electron to hole ratio reaches a maximum of 4.6 (Figure 2.26).

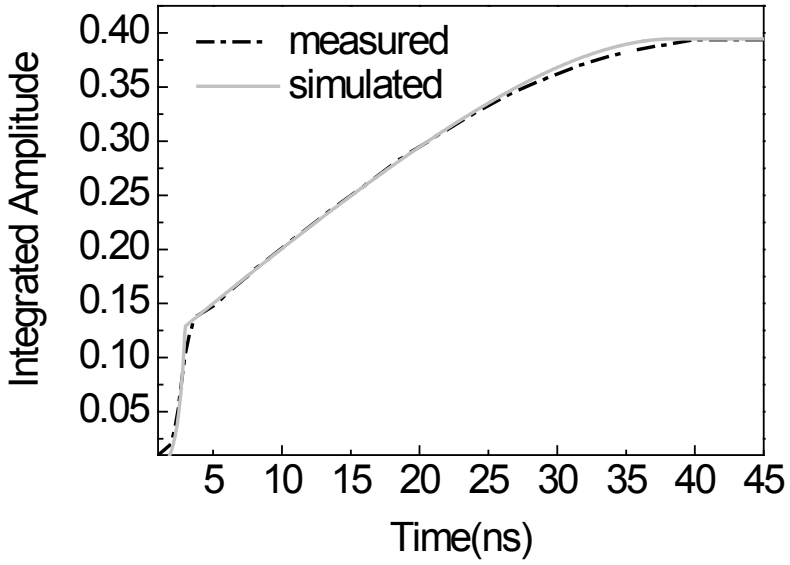

Figure 2.25: Shows the integrated photocurrent and the integral curve obtained by simulation from a-Se HARP blocking structure with RIL (Type 2).

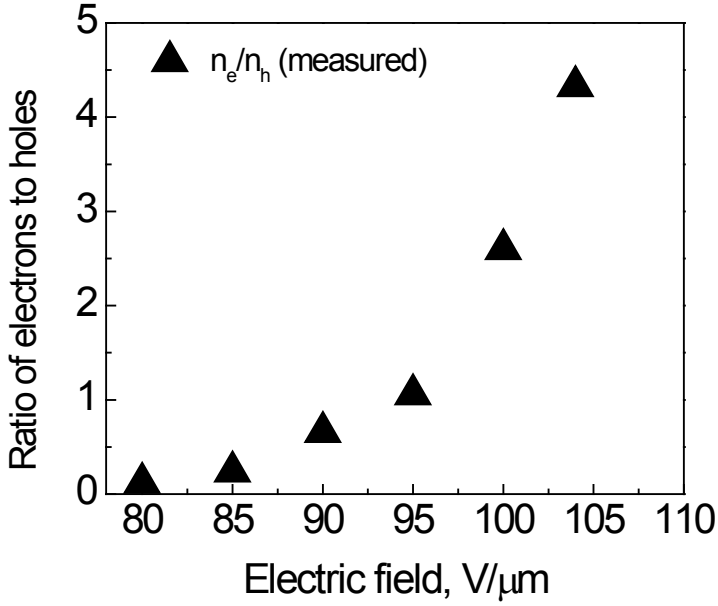

Figure 2.26: The Variation of the ratio of electrons to holes contributing to the TOF signal with applied field calculated from charge collection curves from a-Se HARP blocking structure with RIL (Type 2).

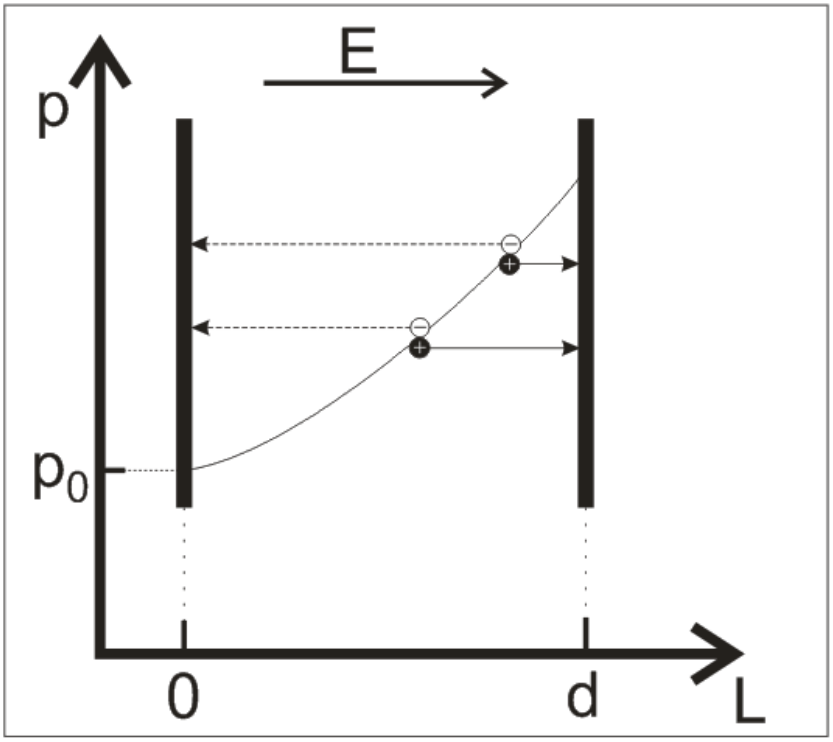

Figure 2.27: Distribution of hole concentration in bulk of a-Se in high electric field where Impact Ionization of holes occurs. Solid line and dash line corresponds to the motion of electrons and holes respectively.

The experimentally measured electron-to-hole ratio provides a convenient method to measure the avalanche gain, g_{AV}, independently of any other parameter. This is possible in a-Se because of the significant difference in the mobilities of holes and electrons as shown above. To derive (n_e/n_h) dependence on g_{AV}, we describe the number of carriers, dn, generated in the layer bounded by x and $x+dx$ by impact ionization by the following differential equation:

$$dn = \gamma_p \cdot n \cdot dx \tag{2.16}$$

With the solution:

$$n(x) = n_0 \exp(\gamma_p x), \tag{2.17}$$

The holes travel forwards a distance (d-x) therefore generating a signal:

$$dn_h^{`} = \frac{d-x}{d} dn \tag{2.18}$$

Similarly, electrons traveling in the opposite direction for a distance x generate a signal:

$$dn_e = \frac{x}{d} dn \tag{2.19}$$

The sum of these two signals gives dn. Combining these equations we obtain:

$$dn_h^{`} = \frac{d-x}{d} n_0 \exp(\gamma_p x)\gamma_p dx \tag{2.20}$$

$$dn_e = \frac{x}{d} n_0 \exp(\gamma_p x)\gamma_p dx \tag{2.21}$$

Which are solved to yield:

$$n_h = n_0 + n_h^{`} = n_0\left(\frac{g_{AV}-1}{\ln g_{AV}}\right) \tag{2.22}$$

$$n_e = \frac{n_0}{\ln g_{AV}}[g_{AV}(\ln g_{AV}-1)+1] \tag{2.23}$$

Since g_{AV} can be expressed as $\frac{n(d)}{n_0}$

The ratio n_e / n_h is then obtained as:

$$\frac{n_e}{n_h} = \left[\left(\frac{g_{AV}}{g_{AV}-1}\right)\ln g_{AV}\right] - 1 \tag{2.24}$$

Equation 2.24 allows us to calculate numerically g_{AV} for a known (n_e / n_h). The results are plotted in Figure 2.28 (open circles). A gain of 200 is achieved at F = 104 V/μm. Further increase in electric field will result in the triggering of electron impact ionization and the self-sustaining avalanche breakdown (Geiger) process [57,41]. To compare, we have calculated g_{AV} with Equation (2.15) using the previously measured field dependence of the hole impact ionization coefficient [59] (Figure 2.28, crosses). The excellent

agreement between measured and calculated results is obvious from Figure 2.28, proving the validity of our approach.

As is evident from Figure 2.29, an excellent agreement was found between gain in the modified HARP structure and the original HARP structure used in HARP tube devices. [59, 40, 43].

Contribution to the TOF signal: the electron to hole ratio theoretical curve was obtained from equation 2.24 and compared to the total gain calculation (figure 2.30). This plot was obtained from Figure 2.26 and Figure 2.28.

Figure 2.30: Contribution to TOF signal, theoretical electrons to holes ratio obtained from Equation 2.24 compared to total gain calculation from Figure 2.28

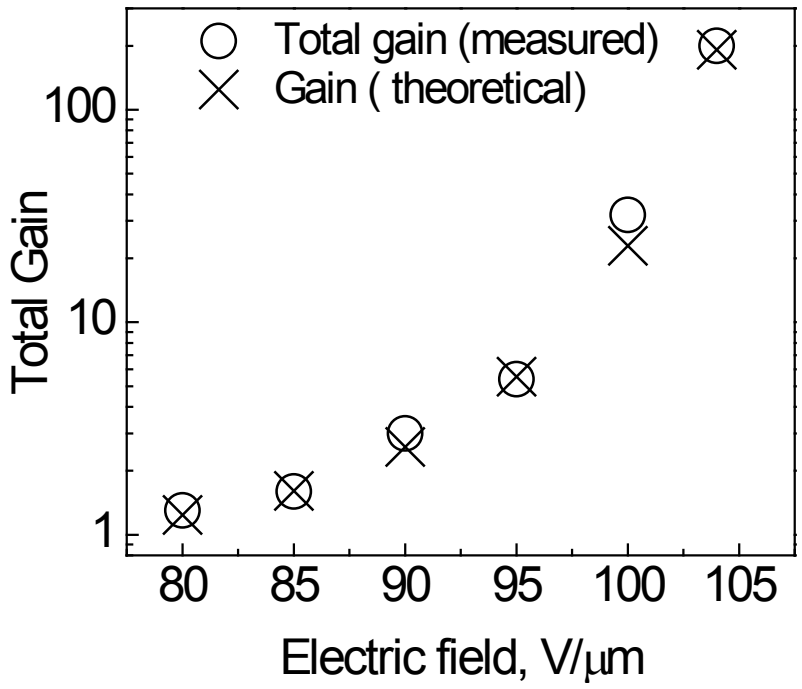

Figure 2.28: The variation of the total gain of holes with the applied field from a-Se HARP blocking structure with RIL (Type 2).

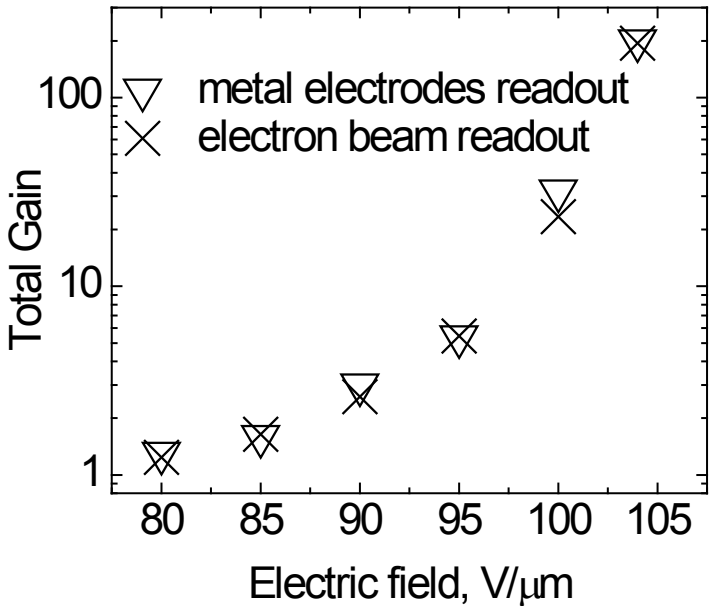

Figure 2.29: Comparison of the total gain of holes to the applied field for sample with electron beam read out system (Figure 2.3) and sample with pixelated structure (Figure 2.2).

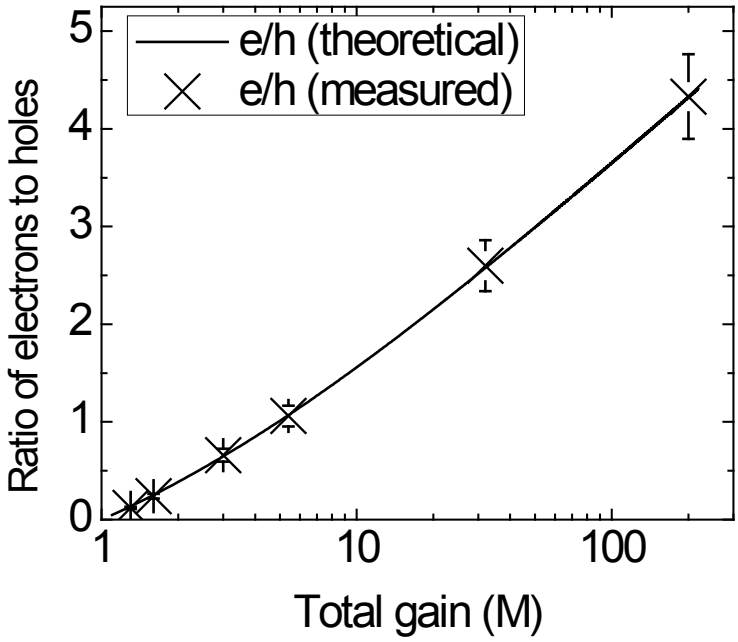

Figure 2.30: Contribution to TOF signal, theoretical electrons to holes ratio compared with measured ratio.

2.6.2. Dark Current kinetics analysis

As mentioned in Section 2.4.2, in an ideal detector, the dark current would be negligibly small. An unacceptably large dark current would cause a number of problems [60]. The noise, i.e., fluctuations in the large dark current, would create noisy pixels (poor signal-to-noise ratio). Such a dark current will constrain the dynamic range by allowing the voltage on the pixel capacitance to build up. Quite often, due to charge carrier trapping and polarization effects, the dark current decays the instant the bias voltage is applied. It is a function of time and the applied nominal field. Therefore, there are variations in the dark current from pixel to pixel. Thus, a large dark current, depending on prior exposure, is difficult to correct and would lead to marked variations in the pixel SNR. Further, in rapid imaging, such as tomosynthesis or PET, there is no time between readouts to correct for adverse effects of the dark current on sensor performance; and hence the dark current limit is even more stringent.

The acceptable dark current depends on the exact application, though values in the range 1–10 pA/mm^2 or 0.1–1 nA/cm^2 are often quoted [60].

Dark current in the case of practical a-Se photoconductors can be reduced to an innocuous level by using thin blocking layers between the a-Se and the electrodes: a single layer of a-Se sandwiched between two electrodes. This identifies the sources of dark current as the injection of holes and electrons from the positive and negative contacts respectively. Thermal generation of electron hole pairs or hole emission from defect states is also possible. For example in the case of a practical low-dark current x-ray photoconductor, there are two thin layers between the a-Se and the electrodes; a "thin" layer refers to the fact that the blocking layer thickness is much smaller than the photoconductor thickness. The hole-trapping layer traps holes and allows electron transport (it is an n-like layer) and the electron-trapping layer traps electrons and allows hole transport (it is a p-like layer). The structure is often referred to as an n-i-p type a-Se photoconductor since the a-Se layer can transport both holes and electrons, resembling an "intrinsic" semiconductor where both carriers play comparable roles. Such terminology is useful and convenient but must be used with care since the Fermi level in a-Se is near the

center of the bandgap, and cannot be easily shifted by doping as in crystalline semiconductors. The required properties are obtained by changing the deep trap concentrations by suitably alloying and doping a-Se with the result that either injected holes or injected electrons are deeply trapped.

In order to prevent charge injection into the photoconductor in the a-Se HARP blocking structure, a blocking layer is used between the photoconductor and the electrode. The blocking layer has material properties that cause the trapping of carriers injected from the contact or creates a high potential barrier for one type of carrier but allow the opposite sign carrier to be transported. Holes injected from the positive contact cannot overcome the high potential barrier created by $Ce0_2$ and electrons injected from the negative contact become trapped in the p-like layer. The space charge is built-up within the p-layer and modifies the field. The actual field at the negative metal contacts are now lower than the corresponding values in the single layer, and hence the rates of electron injection are significantly diminished. The dark current in such multi-layer a-Se photoconductors is about 3 orders of magnitude smaller than that of a single a-Se layer with the same thickness and applied field. In fact, by using blocking structures, dark currents less than 1 pA/mm^2 are routinely obtained for a-Se based photoconductors. It is also possible to reduce the dark current in a-Se photoconductors by a similar amount by modifying the fabrication process itself.

There are two possible sources for dark current in blocking type a-Se photoconductors. First is the rate of actual injection of carriers from the contacts, which would have been reduced more with respect to the injection rate in single layer photoconductors but not zero (the signal current in fact weakens the blocking contact which requires some leakage to keep the contact in equilibrium). The second is the thermal generation in the bulk of the a-Se layer. The thermal generation process is likely to involve a mid-center defect state from which one can emit an electron and hole pair or simply emit only one type of carrier, most likely a hole. The emission of a hole would leave behind an immobile negatively charged center. The latter process controls the decay of the surface electrostatic potential in various a-Se alloy based photoreceptors [61]. Kabir and coworkers at Concordia University [62] have recently modeled the dark current in

multilayer a-Se photoconductors used in x-ray imaging by considering the following. First, the rates of hole and electron injection from the contacts (at metal/a-Se interface) are limited by a Schottky emission rate over some potential barrier for each type of carrier. Second, trapped holes in the n-like layer and electrons in the p-like layer modify the field as does the dark current. Thus, a steady state will eventually be reached. Good agreement has been obtained with experimental results on practical detectors. The model neglects the contribution of thermal generation in the photoconductor, which should also be considered in future modeling, especially in thick a-Se photoconductors.

The above model does not explain and fit the results of dark current kinetics measured on a-Se HARP blocking structures. From our experiments we found out that kinetics of dark current is not affected by the presence of an electron blocking layer ($Ce0_2$) and a RIL. The Dark Current kinetics were measured on all types of samples. However, the kinetics do not depend on the presence of an extra layer (RIL). It also does not depend on the presence of an electron blocking layer. The contact that was used in this measurement is made out of gold, an injecting contact for holes but not for electrons. The work function of gold is around 5.1 eV and the work function of a-Se is around 5 eV measured with the photoelectric effect. Knowing that the Fermi level is in the middle of the a-Se band gap, (2.2 eV) the work function for a-Se from the Fermi level is around 4 eV. This creates a potential barrier for electrons. Further, because the positive voltage was applied to the ITO side of the sample (Figure 2.12), there was no injection of electrons to the bulk of the a-Se from the negative electrode.

For our further analysis, the Type 3 sample (modified uncompleted (no $Ce0_2$) HARP structure with a RIL between the a-Se layer and metal electrode (Au)) was used. The measured dark current kinetics is shown on Figure 2.14. Such kinetics of the dark current in avalanche a-Se can be explained with the idea of draining carriers from the a-Se. The main idea is that the long decay time (~10000) when bias is applied is required to drain all free carriers from the bulk of the a-Se until the equilibrium state is reached (~1 pA/mm^2). Thus, when we short circle the sample and measure the recovery process we must fill the a-Se back up with carriers. In order to verify this, the total collected charge was calculated for both decay (Q_D) and recovery (Q_R). Table 2.1 shows the obtained

results. As it is seen, the total collected charge in the decay and recovery regime is almost identical. This can be a good proof of the validity of this approach. But this has to be further investigated in order to increase our understand of the kinetics.

Table 2.1: shows the total collected charge (Q_D and Q_R) for dark current decay and dark current recovery measurements. As it is seen the amount of total charge is very close. This can be a good prove of validity of this approach.

Electric Field	Q_D for Decay , [pC]	Q_R for recovery, [pC]
10 V/μm	2437	2325
30 V/μm	5150	5670
50 V/μm	7442	8096
60 V/μm	8813	8400

Table 2.2: Shows time constants that were used to do the fitting of Dark Current Decay Kinetics for a-Se "incomplete" HARP blocking structure with RIL.

	τ_1	τ_2	τ_3
30 V/μm	2.4	40.6	212
50 V/μm	2.5	40	210
60 V/μm	2.7	39	206

In order to check time constants used in fitting the Maxwell relaxation time was used:

$$\tau_m = RC = \frac{\varepsilon\varepsilon_0}{\sigma}, \tag{2.25}$$

where R- resistivity, C – capacitance, $\varepsilon = 6.63$ – permittivity of a-Se, $\varepsilon_0 = 8.85\text{x}10^{-12}$ - absolute permittivity and σ – conductivity of a-Se. As conductivity of a-Se is changing with time, it was calculated for different times using the value of current from the experiment (Figure 2.31). The calculated τ_m was found to be almost identical to the fitting parameters in Table 2.2. The similarity in fitting parameters with Maxwell relaxation time for selected dark current densities indicates that relaxation of dark current is due to the Maxwell relaxation time in a-Se.

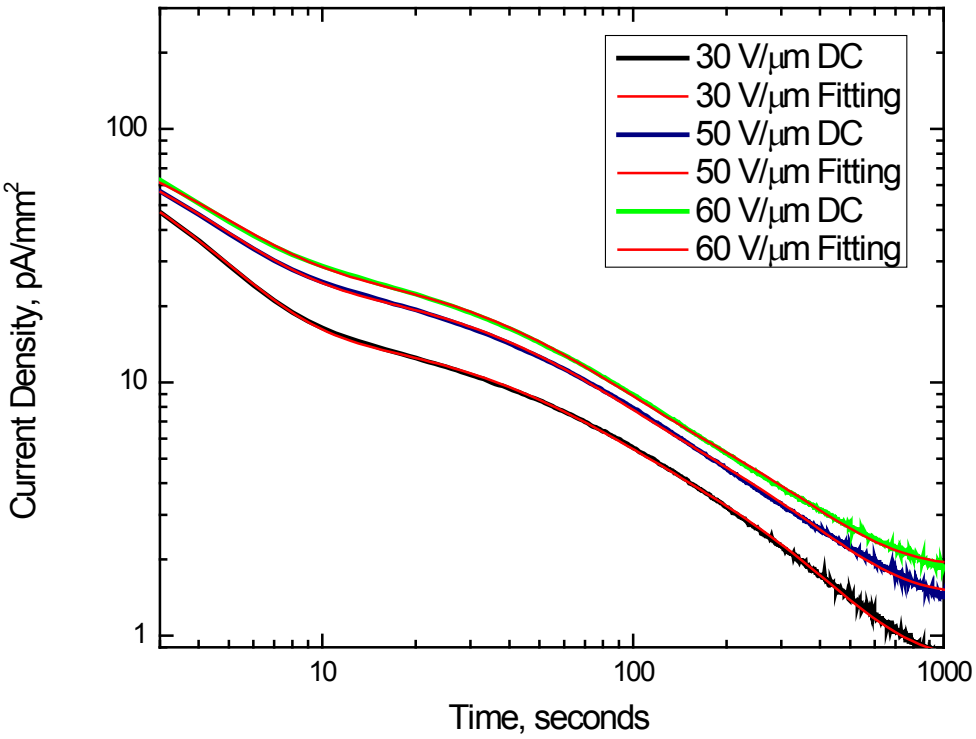

Figure 2.31: Dark Current Decay fitting for a-Se "incomplete" HARP blocking structure with RIL. The fitting is possible with three exponential functions. The time constants used in fitting are the same for all fields.

Figure 2.32 compares the dark currents in a-Se and various other polycrystalline photoconductors, some of which have not yet been tested in a prototype imager. The grey shaded region represents the 1–10 pA/mm^2 range based on the maximum allowed dark current discussion above. What is notable is that the dark current in multilayer a-Se photoconductors is quite small compared to the competing polycrystalline semiconductors. There are very few polycrystalline materials in which the dark current is below the acceptable value for an imaging sensor. We have also indicated the applied field for the reported dark current. It is not possible to simply scale the dark current to the same field in Figure 2.32 inasmuch as the field dependence of the dark current is rarely linear and in many cases it is unknown. The dark current problem in polycrystalline photoconductors has not been fully solved in the sense that one can deposit the layer on

the TFT-AMA, apply a sufficiently large electric field, maintain a low dark current, and achieve good CCE.

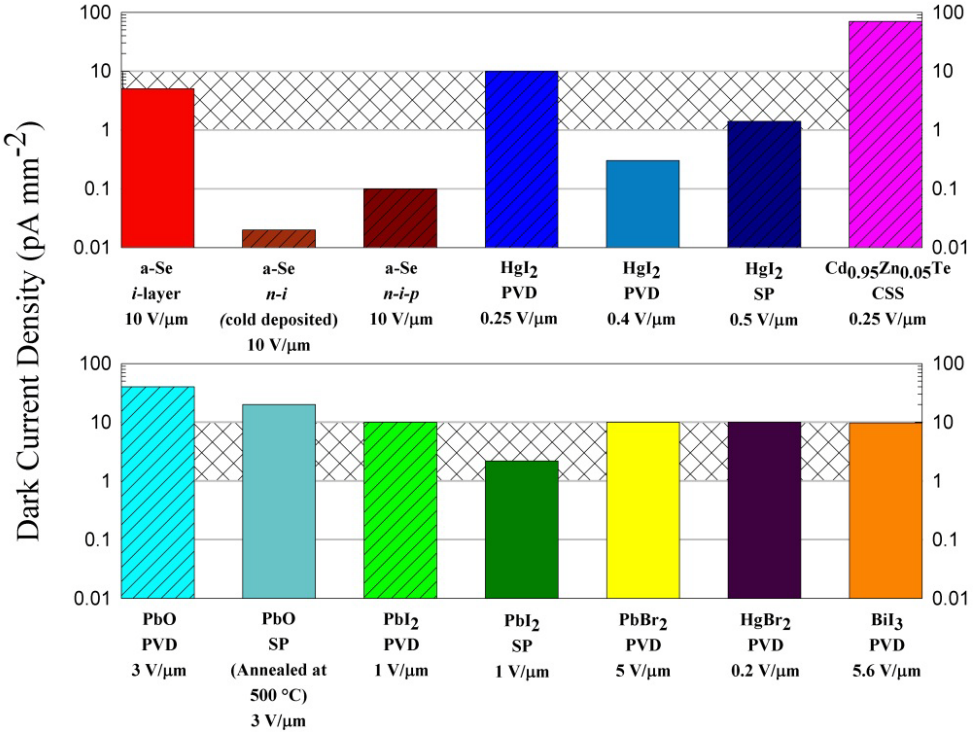

Figure 2.32: The best reported values to date of dark current density for a-Se and polycrystalline photoconductive layers. Note that most of these are measured at relatively low applied electric fields where it is questionable that the charge collection efficiency is adequate. It is not possible to scale these to the same field as the field dependence of the dark current is rarely linear and in general is unknown. All polycrystalline layers are labeled as deposited by physical vapour deposition (PVD), screen printing (SP) or close space sublimation (CSS). Solid colors represent values obtained from films that have not yet been used to obtain x-ray images. The grey hashed area represents the acceptable range for dark curren. Data have been taken from various sources, including the following: a-Se (i-layer and n-i-p) from [63], a-Se (n-i) from [64], HgI_2 (PVD at 0.25 V/µm and SP) from [65], HgI_2 (PVD at 0.4 V/µm) from [66], PbI_2 (PVD) from [67], PbI_2 (SP) from [68], $Cd_{0.95}Zn_{0.05}Te$ from [69], PbO (PVD) from [70], PbO (SP) from [71], $PbBr_2$ and $HgBr_2$ from [72] and BiI_3 from [73].

2.6.3. Amorphous selenium as a PET photodetector

In Section 2.2, the requirements of a detector module were discussed, and it was found that although a-Se has suitable qualities for a photodetector, as it was very successfully utilized in optical imaging. But for a-Se to be successfully utilized in medical imaging,

applications like the PET electron beam readout have to be replaced by the two dimensional metal pixel electrode arrays. This thesis shows practical solutions for avalanche a-Se photosensors with electrode structures. With our samples we measured important parameters of a-Se. Specifically, we are interested in the transport properties (CCT and rise time) and avalanche gain.

1. Charge collection time -The CCT is the time required for a photodetector to completely collect all the photogenerated charges, which depends on when charge carriers are created, their drift velocity and the distance they need to travel to reach the electrodes. CCT is important because it affects the detector dead time of a detector module. Using our TOF measurements, we can see the CCT for an impulse excitation for various fields.

The CCT depends on the thickness of the a-Se and the electric field applied. CCT decreases as the thickness of the a-Se layer decreases because of the shorter distance travelled by the charge carriers. The CCT also decreases as the field is increased because of the increase in charge carrier velocity. However, what's interesting is the boundary between the sub-avalanche and the avalanche regions. In the sub-avalanche region, there is no impact ionization; all the photogenerated charge carriers are created near the anode, and the holes drift towards the cathode at a speed determined by their mobility. The transient current has a simple rectangular shape as shown in Figure 2.9, and the CCT is simply the thickness divided by hole velocity. On the other hand, in the avalanche region, impact ionization creates EHPs throughout the a-Se layer in addition to the photogenerated charge carriers. Compared to the sub-avalanche region, the CCT in avalanche region extends by the time required for the electrons that are created near the cathode to drift back towards the anode.

Assuming operation at F = 104 V/μm for maximum gain and the fastest response, the CCT is on the order of 35 to 40 ns depending on thickness. The CCT is thus comparable to the decay constant of 40 to 300 ns of common PET scintillators and does not represent a limiting factor.

2. Rise time - The rise time is defined as the time required for the impulse response to increase from 10% to 90% of the peak value. A fast rise time is important for accurate time pick -off as it minimizes time jitter, which in turn improves the timing resolution of the detector module. A rise time of less than 1 ns is obtained in avalanche regime from TOF photo response (Figure 2.10). The shape of the curves is counter intuitive which is mainly a result of having an exponentially increasing peak in the transient current (shown in Figure 2.10) and the assumption that charge carriers reach their drift velocities as soon as they are created. At lower fields where there is very little avalanche gain, the rise time increases rapidly with the field and then appears to approach an asymptote. This shape is a consequence of the assumed infinite acceleration. As soon as the charge carriers are created, they instantaneously reach their drift velocities, bringing the transient current to a level above 10% of the peak at time zero. Therefore, this part of the curves essentially shows the time required for the signal to reach 90% of the peak from time zero.

At higher fields, an exponential decrease in the rise time is observed. In this part of the curve, the gain is sufficiently high that the assumed infinite acceleration of charge carriers during photogeneration no longer brings the transient current to above 10% of the peak value. In other words, the time required for the signal to reach 10% of the peak is "catching up" to the 90% time, making the rise time shorter. Although the rise time is much shorter at lower fields, the avalanche gain at these fields is too small to be useful. Thus, rise time must be sacrificed for higher avalanche gain. Our results show that at a high gain *(F = 104 V/μm),* the rise time was < 1 ns for the thicknesses considered. This value is comparable to the rise time achievable by PMTs and Si APDs. Together with a short TTS, it is expected that the timing resolution of a-Se photodetectors is comparable to PMTs and Si APDs.

3. Avalanche gain - A large gain is necessary to increase the SNR of the photo detector output. With our avalanche gain measurements, the total gain for different fields is plotted in Figure 2.22. The maximum theoretical gain was achieved for 15 μm a-Se layer thickness at F= 104 V/μm. It is important to mention that with the 35 μm a-Se layer thickness, a gain of 1000 can be achieved at $F = 92$ *V/μm*. Although the gain is less than the typical gain of 10^6 in a PMT, it is higher than the typical gain in Si APDs.

Furthermore, the dark current in a-Se is smaller than in Si because of the wider band gap. (2.2 eV for a-Se compared to 1.12 eV for Si) These properties make a-Se more attractive than Si APDs.

2.7. Conclusion

The results on transport properties of the modified a-Se HARP structure show that a Resistive Interface Layer (RIL) made of Cellulose Acetate (CA) is a practical solution for the implementation of metal electrodes to avalanche a-Se photosensors: it improves stability against dielectric breakdown while not affecting transport properties. Moreover, the modified a-Se HARP structure is characterized by extremely low dark current. The combination of low dark current with high avalanche multiplication gain makes avalanche a-Se photosensor a promising alternative to silicon avalanche photodiodes (APD) for a variety of applications in medical imaging.

Chapter 3 Future work

3.1.Summary of thesis

The results on transport properties of the modified a-Se HARP structure show that a Resistive Interface Layer (RIL) made of Cellulose Acetate (CA) can be used to improve stability against a dielectric breakdown, and is a practical solution for the implementation of metal electrodes to avalanche a-Se photosensors. We show that both the modified (with the RIL) and the original HARP devices exhibit almost identical charge transport and avalanche gain, which means that the RIL does not degrade a-Se transport properties while enabling its stable operation in the avalanche regime, protecting it against breakdown. A gain of 200 at 104 V/μm has been demonstrated for the modified HARP structure with a 15 μm thick a-Se layer, which is the maximum theoretical gain for this thickness [30, 12]. Moreover, the shape of the photocurrent and the field dependence of the hole mobility in the modified HARP are shown to be identical to those obtained in the "prototype" insulating a-Se samples by Juska and Arlauskas [57,58], who discovered avalanche multiplication in a-Se in the early 80's using metal/polymer/a-Se/polymer/metal sandwiched structures. In contrast to the insulating a-Se structure, which cannot be used as a practical avalanche photosensor as no exit of mobile carriers is allowed, the presented modified a-Se HARP structure is the first practical approach to the a-Se avalanche photosensor with metal electrodes. We believe that the modified HARP represents the future of a-Se photodetectors in radiation medical imaging in both direct conversion detectors for low energy applications (like protein crystallography) and in indirect conversion detectors (like PET).

3.2. Prototype a-Se-based PET detector module

The experimental work presented in this thesis showing that avalanche a-Se photodetectror with a RIL has a huge potential in replacing conventially used PMTs in PET block detector modules. Therefore, the next step in the development of an a-Se-based detector module is to build a prototype detector in order to evaluate its performance. The simplest prototype involves coupling a scintillator to an a-Se layer. The

advantage of using only one photodetector is that the readout is simple; both energy and timing resolution can be measured without implementing the extra circuitry necessary for adding and comparing signals for two photodetectors. The measured energy and timing resolution can also be directly compared to those obtained with a PMT/scintillator module. Because the dimensions of a scintillator can affect the optical coupling and light collection efficiency, the crystal scintillator should be long and narrow. All but one side of the scintillator should be rapped in light reflecting tape to maximize light collection by the photodetector. The scintillator should be firmly fixed to the photodetector with optical grease to eliminate any air gaps between the crystal and the photo conductor that might degrade light transmission efficiency. The entire detector module must be put in a light-tight enclosure to ensure that ambient light is not detected by the photodetector. The schematic of PET block detector based on a-Se photodetector is shown in Figure 3.1.

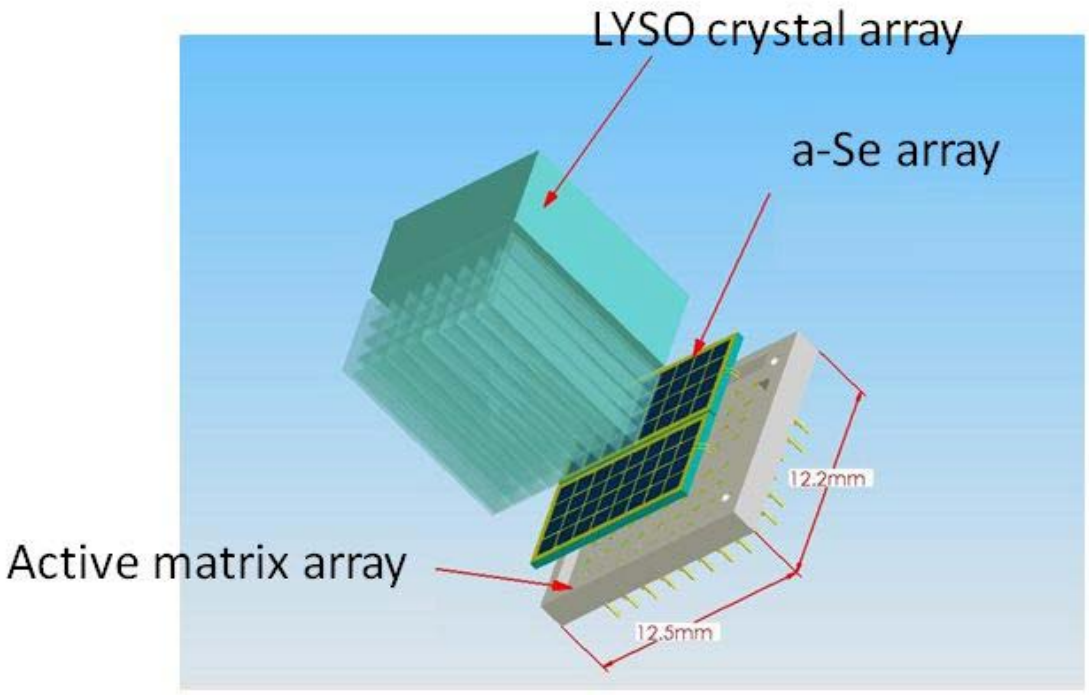

Figure 3.1: a-Se based PET detector design. In this design a-Se is deposited on active matrix array and other side is optically coupled to LYSO scintallation crystall.

In the presented detector block design resolution of the detector will be limited by the pixel size. Improving existing detector block for PET by replacing PMTs with avalanche

a-Se photosensor will result in overall increase of sensitivity, reduced price and will lead to a new era of magnetic field compatible PET systems.

3.3. Applications of the a-Se photodetector module

The a-Se photodetector module is a general PET detector module that can be applied to different PET configurations. The primary benefits of this detector module, compared to the traditional PMT-based block detector, are its small pixels, and low cost as well as rigid, small and magnetic field compatible design. These benefits have the potential to increase spatial resolution and enable systems with better γ-ray detection efficiency. The overall spatial resolution of PET images is improved by the smaller pixel size. Also, smaller-diameter or organ-specific PET scanners that have higher γ-ray detection efficiency can be designed without sacrificing spatial resolution uniformity. Finally, the cost of the detector module is expected to be lower with the use of a-Se, and the detector module assembly can be made more compact without the bulky PMTs.

While it can be used to reduce the cost and improve the performance of whole-body (WB) PET, scanners that will benefit the most from this detector in terms of image quality are likely to be small-animal or organ-specific, such as the brain and breast, PET scanners. An example of an organ-specific PET scanner that benefits from the a-Se-based detector module is a positron emission mammography (PEM) system [74]. PEM is a PET scanner dedicated to the imaging of the breast. Instead of a large detector ring surrounding the patient, a PEM scanner consists of parallel-plate detectors on both sides of a compressed breast, similar to x-ray mammography. PEM has many advantages over WB PET. Placing the parallel-plate detectors against the breast implies high solid-angle coverage, resulting in better γ-ray detection efficiency. The field of view (FOV) is also limited to the volume between the plates, reducing unwanted scatter from the rest of the body. Furthermore, the compressed breast results in less γ-ray scattering by the soft tissue and less patient motion. However, although more γ-rays are detected, a large fraction of them will strike the detectors at an angle because of the parallel-plate geometry. This results in significant parallax errors across the entire FOV, degrading spatial resolution. The depth of interaction capability of the a-Se-based dual photodetector module is therefore an important feature that will be able to eliminate this problem. The small

pixels will also result in better spatial resolution, which is critical in the diagnosis of breast cancer.

Another application of the a-Se photodetector module is in the area of combined PET/MRI scanners. In contrast to x-ray CT, MRI is able to provide extra information of the patient from techniques such as functional MRI (f-MRI) and Diffusion Tensor Imaging (DTI) in addition to high resolution anatomical images. Combining these modalities in the same system allows simultaneous acquisition of both images and easier co-registration. The traditional PMT-based block detector is sensitive to magnetic fields and is not suitable for a PET/MRI scanner. On the other hand, the a-Se photo detector module does not contain any magnetic field-sensitive components, making it suitable for *PET/MR* scanners.

We believe that the proposed a-Se-based photodetector module is superior to the block detector and has the potential to improve both the image quality and the practicality of different types of PET imaging. Further studies must be done to optimize the design parameters of the block detector module for different PET applications. The improved PET scanners will make PET an even more attractive tool in clinical and research environments.

Bibliography

1) J. Beutel, H. L. Kundel and R. L. Van Metter, Handbook of Medical Imaging, (SPIE Press, 2000).

2) G.L. Brownell, W.H. Sweet, "Localization of brain tumors with positron emitters," Nucleonics 11,40-45 (1953).

3) W.H. Sweet, "The uses of nuclear disintegration in the diagnosis and treatment of brain tumor," N. Engl. J. Med. 245, 875-878 (1951).

4) F.R. Wrenn, M.L. Good, P. Handler," The use of positron-emitting radioisotopes for the localization of brain tumors," Science 113, 525-527 (1951).

5) M.E. Phelps, E. Hoffinan, N. Mull ani, C. Higgins, M. Ter-Pogossian, "Design considerations for a positron emission transaxial tomograph (PET III)," IEEE Trans. Biomed. Eng. NS-23, 516-522 (1976).

6) C. L. Melcher, "Scintillation Crystals for PET"J. Nucl. Med. 41, 1051 – 1055 (2000).

7) Casey ME, Nutt R. "A multicrystal two dimensional BGO detector system for positron emission tomography". IEEE Trans Nucl Sci. 33, 460-463, (1986)

8) R. Nutt, "The history of positron emission tomography," Mol. Imaging and BioI. 4, 11-26 (2002).

9) T. Ido, C.N. Wan, V. Casella, J.S. Fowler, A.P. Wolf, M. Reivich, and D.E. Kuhl, J. of Labelled Compounds and Radiopharmaceuticals 14, 175-183 (1978).

10) S.S. Gambhir, J. Czemin, J. Schwimmer, D.H.S. Silverman, R.E. Coleman, and M.E. Phelps, "A tabulated summary of the FDG PET literature," J. Nucl. Med. 42, 1S-93S (2001).

11) M. Furuta et al., “Basic evaluation of a C-shaped breast PET scanner,” in 2009 IEEE Nucl. Sci. Symp. Conf. Rec., pp. 2548–2552 (2009).

12) E. Albuquerque et al., “Charaterization of the clear-PEM breast imaging scanner performance,” in 2009 IEEE Nucl. Sci. Symp. Conf. Rec., pp. 3487–3490 (2009).

13) M. Mahesh, “MDCT Physics: The Basics--Technology, Image Quality and Radiation Dose”, Chapter 9, p 151 (2009)

14) S.R. Cherry, J.A. Sorenson, M.E. Phelps, Physics in Nuclear Medicine, 3rd ed. (Saunders, Philadelphia, 2003).

15) M.E. Casey and R Nutt, "A multi crystal two dimensional BGO detector system for positron emission tomography," IEEE Trans. Nucl. Sci. NS-33, 460-463 (1986).

16) D. W. Townsend, “Physical Principles and Technology of Clinical PET Imaging”, Annals Academy of Medicine, 33, 133-145 (2004)

17) M.E. Phelps, PET: Molecular Imaging and Its Biological Applications (Springer-Verlag New York, New York, (2004).

18) F. Habte, A. M. K. Foudray, P. D. Olcott and C. S. Levin, “Effects of system geometry and other physical factors on photon sensitivity of high-resolution positron emission tomography”, Phys. Med. Biol, 52, 3752-3772 (2007)

19) L.R MacDonald and M. Dahlbom, "Parallax correction in PET using depth of interaction information," IEEE Trans. Nucl. Sci., 45, 2232-2237 (1998).

20) Canadian Cancer Society/National Cancer Institute of Canada: Canadian Cancer Statistics 2007, Toronto, Canada, (2007).

21) M. Colleoni *et al,* “Minimal and small size invasive breast cancer with no axillary lymph node involvement: the need for tailored adjuvant therapies”, Annals of Oncology, 15, 1633-1639 (2004).

22) Thompson, C. J., K. Murthy, I. N. Weinberg, and F. Mako, Feasibility study for positron emission mammography. Medical physics 21:529-538 (1994).

23) Raylman, R. R., S. Majewski, A. G. Weisenberger, V. Popov, R. Wojcik, B. Kross, J. S. Schreiman, and H. A. Bishop. Positron emission mammography-guided breast biopsy. J Nucl Med 42:960-966 (2001).

24) D. Schlyer, W. Rooney, C. Woody, P. Vaska, A. Kriplani, S. Stoll, "Development of a simultaneous PET/MRI scanner," IEEE Nucl. Sci. Symposium Conf. Rec. 6, 3419 – 3421 (2004).

25) B.J. Pichler, M.S. Judenhofer, C. Catana, J.H. Walton, M. Krieilling, RE. Nutt, S.B. Siegel, C.D. Claussen, and S.R. Cherry, "Performance Test of an LSO-APD Detector in a 7-T MRI Scanner for Simultaneous PET/MRI," J. Nucl. Med. 47, 639-647 (2006).

26) Kasap, S.; Rowlands, J.A.; Baranovskii, S.D.; Tanioka, K. Lucky drift impact ionization in amorphous semiconductors. J. Appl. Phys,, 96, 2037-2048 (2004).

27) Reznik, A.; Baranovskii, S.D.; Rubel, O.; Juska, G.; Kasap, S.O.; Ohkava, Y.; Tanioka, K; Rowlands, J.A. Avalanche multiplication phenomenon in amorphous semiconductors: Amorphous selenium versus hydrogenated amorphous silicon. J. Appl. Phys., 102, 053711-053717 (2007).

28) Jandieri, K.; Rubel,O.; Baranovskii, S.D.; Reznik, A.; Rowlands, J.A.; Kasap, S.O. Lucky-drift model for impact ionization in amorphous Semiconductors. J. Mater. Sci. Mater. Electron., 20, S221-S226 (2009).

29) Juska, G.; Arlauskas, K. Phys. Features of hot carriers in amorphous selenium. Phys. Status Solidi A Appl. Mat. Sci., 77, 387-391 (1983).

30) Reznik, A.; Baranovskii, S.D.; Rubel, O.; Jandieri, K.; Rowlands, J.A. Photoconductivity in amorphous selenium blocking structures. Phys. Status Solidi C Curr. Top. Solid State Phys., 5, 790-795 (2008).

31) Hunt, D.C.; Kirby, S.S.; Rowlands, J.A. X-ray imaging with amorphous selenium: X-ray to charge conversion gain and avalanche multiplication gain. Med. Phys., 29, 2464-2471 (2002).

32) Lui, B.J.M.; Hunt, D.C.; Reznik, A.; Tanioka, K.; Rowlands, J.A. X-ray imaging with amorphous selenium: pulse height measurements of avalanche gain fluctuations. Med. Phys., 33, 3183-3192 (2006).

33) Hunt, D.C.; Tanioka, K.; Rowlands, J.A. X-ray imaging using avalanche multiplication in amorphous selenium: Investigation of intrinsic avalanche noise. Med. Phys., 34, 4654-4663 (2007).

34) Hunt, D.C.; Tanioka, K.; Rowlands, J.A. X-ray imaging using avalanche multiplication in amorphous selenium: investigation of depth dependent avalanche noise. Med. Phys., 34, 976-986 (2007).

35) Reznik, N.; Komljenovic, P.T.; Germann, S.; Rowlands, J.A. Digital Radiography using amorphous selenium: Photoconductively activated switch (PAS) readout system. Med. Phys., 35, 1039-1050 (2008).

36) Wronski, M.M.; Zhao, W.; Reznik, A.; Tanioka, K.; DeCrescenzo, G.; Rowlands, J.A. A solid-state amorphous selenium avalanche technology for large area photon counting and photon starved imaging applications. Med. Phys. Lett., 37, 4982-4986 (2010).

37) Sultana, A.; Reznik, A.; Karim, K.S.; Rowlands, J.A. Design and feasibility of active matrix flat panel detector using avalanche amorphous selenium for protein crystallography. Med. Phys., 35, 4324-4332 (2008).

38) Sultana, A.; Karim, K.S.; Rowlands, J.A. The effect of K-fluorescence reabsorption of Selenium on the performance of an imaging detector for protein crystallography. Phys. Status Solidi C Curr. Top. Solid State Phys., 6, S231-S235 (2009).

39) A. Reznik, B.J.M. Lui, Y. Ohkawa, T. Matsubara, K. Miyakawa, M. Kubota, K. Tanioka, T. Kawai, W. Zhao, J.A. Rowlands, NuclInstrum Methods Phys Res A 567 93 (2006).

40) A. Reznik , S.D. Baranovskii, O. Rubel, K. Jandieri, S.O. Kasap, Y. Ohkawa, M. Kubota, K. Tanioka, J.A. Rowlands, Journal of Non-Crystalline Solids 354 2691 (2008).

41) A. Reznik, W. Zhao, Y. Ohkawa, K. Tanioka , J. A. Rowlands J Mater Sci: Mater Electron 20 S63–S67 (2009).

42) K. Tanioka, J. Yamazaki, K. Shidara, K. Taketoshi, T. Kawamura, S. Ishioka, and Y. Takasaki, IEEE Electron Device Lett. 8 392 (1987).

43) J. Yamazaki, M. Kubota, H. Maruyama, K. Tanioka, K. Shidara, T. Hirai, K. Tsuji, Y. Takasaki, and M. Yamamoto, Television Gakkai-shi 46 1189 (1992).

44) Y. Ohkawa, K. Miyakawa, T. Matsubara, K. Kikuchi, S. Suzuki, M. Kubota, N. Egami, and A. Kobayashi, Phys.Status Solidi C 6/S1 S224-S226 (2009).

45) A. Reznik, S. D. Baranovskii, O. Rubel, K. Jandieri, and J. A. Rowlands, Phys. Stat Sol (c) 5 790 (2008).

46) S. Kasap, J.B. Frey, G. Belev, O. Tousignant, H. Mani, L. Laperriere, A. Reznik, and J. A. Rowlands. Phys. Status Solidi B 246 1794–1805 (2009).

47) E. Maruyama, Japanese Journal of Applied Physics 21–2 213 (1982).

48) Tanioka, K.; Yamazaki, J.; Shidara, K.; Taketoshi, K.; Kawamura, T.; Ishioka, S.; Takasaki, Y. An avalanche-mode amorphous Selenium photoconductive layer for use as a camera tube target. IEEE Electron Dev. Lett., 8, 392-394 (1987).

49) Ohkawa, Y.; Miyakawa, K.; Matsubara, T.; Kikuchi, K.; Suzuki, S.; Kubota, M.; Egami, N.; Kobayashi, A. Temperature dependence of carrier traps in high sensitivity

HARP photoconductive film. Phys. Status Solidi C Curr. Top. Solid State Phys., 6, S224-S226 (2009).

50) Kubota, M.; Kato, T.; Suzuki, S.; Maruyama, H.; Shidara, K.; Tanioka, K.; Sameshima, K.; Makishima, T.; Tsuji, K.; Hirai, T.; Yoshida, T. Ultrahigh-sensitivity new Super-HARP camera. IEEE Trans. Broadcast., 42, 251-258 (1996).

51) T. Ohshima, K. Tsuji, K. Sameshima, T. Hirai, K. Shidara, and K. Taketoshi, "Excess Noise in Amorphous Selenium Avalanche " Japanese Journal of Applied Physics 30 (6B), L1071-L1074 (1991).

52) Y. Takiguchi, H. Maruyama, M. Kosugi, F. Andoh, T. Kato, and K. Tanioka, "A CMOS Imager Hybridized to an Avalanche Multiplied Film," IEEE Trans. Electronic Devices 44 (10), 1783- 788 (1997).

53) M. Wronski, Development of a flat panel detector with avalanche gain for interventional radiology, Thesis, (2009).

54) M. Wronski, W. Zhao, A. Reznik, K. Tanioka, G. Decscenzo, J. A. Rowlands, A solid state amorphous selenium avalanche technology for low photon flux imaging applications. Med. Phys. 37 9 (2010).

55) T. S. Curry, J. E. Dowdey, and R. C. Murry, Christensen's Physics of Diagnostic Radiology (Lipnicott Williams & Wilkins, 1990), fourth ed.

56) R.A. Street, Hydrogenated amorphous silicon, edited by R.W. Cahn, E.A. Davis and I.M. (Ward, Cambridge University Press), Chap. 3, 62-95 (1991).

57) G. Juska, K. Arlauskas, Phys. Stat Sol (a) 77 387 (1983).

58) G. Juska, K. Arlauskas, Impact ionization and mobilities of charge carriers at high electric fields in amorphous selenium, Phys. Stat Sol (a) 59 389-393 (1980).

59) A. Reznik, S.D. Baranovskii, O. Rubel, G. Juska, S. Kasap, Y.Ohkawa, K. Tanioka, J.A. Rowlands, J. Appl. Phys. 102 053711 (2007).

60) Kasap, S.O.; Rowlands, J.A. Direct-conversion flat-panel x-ray image detectors. IEEE Proc. Circ. Dev. Syst., 149, 85-96 (2002).

61) Kasap, S.O. Dark decay of electrostatic surface potential on dielectrics via bulk space charge buildup. J. Electrostat., 22, 66-90 (1988).

62) Mahmood, S.A.; Kabir, M.Z.; Tousignant, O.; Mani, H.; Greenspan, J.; Botka, P. Dark current in multilayer amorphous selenium x-ray imaging detectors. Appl. Phys. Lett., 92, 223506-223509 (2008).

63) Kasap, S.; Frey, J.B.; Belev, G.; Tousignant, O.; Mani, H.; Laperriere, L.; Reznik, A; Rowlands, J.A. Amorphous selenium and its alloys from early xeroradiography to high resolution x-ray image detectors and ultrasensitive imaging tubes. Phys. Status Solidi B Basic Solid State Phys., 246, 1794-1805 (2009); (and references therein).

64) Belev, G.; and Kasap, S.O. Reduction of the Dark Current in Stabilized a-Se Based X-Ray Detectors. J. Non-Cryst. Solid., 352, 1616-1620 (2006).

65) Du, H.; Antonuk, L.E.; El-Mohri, Y.; Zhao, Q.; Su1, Z.; Yamamoto, J.; Wang, Y. Investigation of the signal behavior at diagnostic energies of prototype, direct detection, active matrix, flat-panel imagers incorporating polycrystalline HgI2. Phys. Med. Biol., 53, 1325-1351 (2010).

66) Fornaro, L.; Cuña, A.; Noguera, A.; Aguiar, I.; Pérez, M.; Mussio, L.; Gancharov, A. Low Dark Current (0 0 l) Mercuric Iodide Thick Films for X-Ray Direct and Digital Imagers. IEEE Trans. Nucl. Sci., 52, 3107-3110 (2006).

67) Street, R.A.; Ready, S.E.; van Schuylenbergh, K.; Ho, J.; Boyec, J.B.; Nylen, P.; Shah, K.; Melekhov, L. Comparison of PbI2 and HgI2 for direct detection active matrix x-ray image sensors. J. Appl. Phys., 91, 3345 (2002).

68) Yun, M.; Cho, S.; Lee, R.; Jang, G.; Kim, Y.; Shin, W.; Nam, S. Investigation of Pbi2 film fabricated by a new sedimentation method as an x-ray conversion material. Jpn. J. Appl. Phys., 49, 041801-041805 (2010).

69) Tokuda, S.; Kishihara, H.; Adachi, S.; Sato, T. Preparation and characterization of polycrystalline CdZnTe films for large-area, high-sensitivity X-ray detectors. J. Mater. Sci. Mater. Electron., 5, 1-8 (2004).

70) Simon, M.; Ford, R.A.; Franklin, A.R.; Grabowski, S.P.; Mensor, B.; Much, G.; Nascetti, A.; Overdick, M.; Powell, M.J.; Wiechert, D.U. PbO as direct conversion x-ray detector material. Proc. SPIE, 5368, 188-199 (2004).

71) Cho, S.; Kang, S.; Kwon, C.; Yun, M.; Park, J.; Park, S.; Choi, J.; Mun, C.; Lee, H.; Nam, S. Effect of Anealing on the X-ray Detection Properties of Nano-sized Polycrystalline Lead Oxide Films. Jpn. J. Appl. Phys., 47, 7393-7397 (2008).

72) Fornaro, L.; Sasen, N.; Pérez, M.; Noguera, A.; Aguiar, I. Comparison of mercuric bromide and lead bromide layers as photoconductors for direct X-ray imaging applications. IEEE Nucl. Sci. Symp. Confer. Rec., 3750-3754 (2006).

73) Aguiar, I.; Kröger, S.; Fornaro, L. Bismuth tri-iodide polycrystalline films for X-ray direct and digital imagers. Nucl. Instrum. Meth. Phys. Res. A, 610, 332-334 (2009).

74) A. Reznik, B.J.M. Lui, J.A. Rowlands, "An amorphous selenium based positron emission mammography camera with avalanche gain," Tech. in Cancer Research & Treatment 4, 1-7 (2005).